3D FORWARD MODELING AND PARAMETRIC INVERSION OF INDUCED POLARIZATION WITH ELECTROMAGNETIC COUPLING

by

Deniz Donmez

A thesis submitted to the Faculty and the Board of Trustees of the Colorado School of Mines in partial fulfillment of the requirements for the degree of Master of Science (Geophysics).

Golden, Colorado

Date _____

Signed: _____
Deniz Donmez

Signed: _____
Dr. Andrei Swidinsky
Thesis Advisor

Golden, Colorado

Date _____

Signed: _____
Dr. Paul Sava
Professor and Head
Department of Geophysics

ABSTRACT

The induced polarization (IP) method is commonly used in mineral exploration. In particular, it has been successfully applied to explore for disseminated sulfide and/or porphyry deposits, which often have strong induced polarization responses. IP methods can provide information about the chargeability and resistivity distribution of the subsurface. However, these methods may underperform under certain geological conditions, such as in the presence of highly conductive or resistive cover. In the presence of resistive cover, the direct current (DC) signal cannot penetrate beneath this zone, and in the presence of conductive cover, a short circuit results. In such cases, the inductive response of the Earth can potentially contain information about the subsurface geological units due to complimentary physics to the DC resistivity method. This is because the current flow generated by electromagnetic (EM) induction can penetrate resistive features. However, EM coupling is generally considered to be noise and unwanted content in the DC/IP signal. In the traditional processing and interpretation of IP data, inductive effects are usually eliminated.

Although removing the electromagnetic effect to increase the sensitivity to IP signal is the main focus of the mineral exploration industry, there is a possibility to extract more information about the subsurface by using EM induction. However, in order to handle this multi-parameter physical problem, traditional DC/IP modeling is deficient. Moreover, the conductivity model needs to be defined by a frequency or time-dependent complex conductivity. Throughout this thesis, we investigate the relationship between IP and EM by simulating grounded source time-domain DC/EM/IP data with a complex conductivity model called the stretched exponential with SimPEG and SimPEG EMIP. This method allows us to model IP relaxation in the time-domain instead of using the Cole-Cole model (CC) in the frequency-domain. Cole-Cole in the frequency-domain is a standard approach in the context of complex conductivity modeling. However, it is computationally expensive to ap-

ply in time-domain since Fourier transform is needed. With the stretched exponential, one can simulate a grounded source time-domain DC/EM/IP survey with complex conductivity more efficiently.

We used different geoelectrical models such as a chargeable conductive block in a resistive subsurface, a chargeable resistive block in a conductive subsurface, a chargeable conductive block buried under a relatively conductive cover, a chargeable conductive block buried under a relatively resistive cover, and a 3D porphyry-mineral deposit model. By using the full DC/EM/IP step response, we calculated apparent resistivities by using the peak arrival time of the signal obtained from normalized pseudoimpulse response. Our results show that this method contains more information about the subsurface than the traditional DC/IP method. Furthermore, we apply a parametric inversion to a simple block model and show that grounded source DC/EM/IP data with complex conductivity can be inverted. However, a full 3d inversion is necessary to characterize this highly non-unique and difficult EM problem.

TABLE OF CONTENTS

LIST OF FIGURES

LIST OF TABLES

LIST OF SYMBOLS

Angular Frequency . . . . . ω (rad/s)

Chargeability . . . . . η (V/V)

Current Density (Time Domain, Frequency Domain) . . . . . $\vec{j}$, $\vec{J}$ (A/m^2)

Dielectric Permittivity . . . . . ϵ (F/m)

Electrical Conductivity . . . . . σ (S/m)

Electric Current . . . . . I (A)

Electric Field (Time Domain, Frequency Domain) . . . . . $\vec{e}$, $\vec{E}$ (V/m)

Frequency Exponent . . . . . c (Unitless)

Magnetic Field (Time Domain, Frequency Domain) . . . . . $\vec{h}$, $\vec{H}$ (A/m)

Magnetic Flux Density (Time Domain, Frequency Domain) . . . . . $\vec{b}$, $\vec{B}$ (T)

Magnetic Permeability . . . . . μ (H/m)

Normalized Pseudoimpulse Peak Arrival Time . . . . . τ_{EM} (s)

Resistivity . . . . . ρ (Ωm)

Time Constant of The Decay . . . . . τ_{IP} (s)

Voltage . . . . . V (V)

LIST OF ABBREVIATIONS

Airborne Time-Domain Electromagnetic Methods . . . . . ATEM

Cole-Cole Model CC

Electromagnetic Induction and Induced Polarization . . . . . EM/IP

Direct Current . . . . . DC

Direct Current - Induced Polarization . . . . . DC/IP

Direct Current - Electromagnetic - Induced Polarization . . . . . DC/EM/IP

Electromagnetic Methods . . . . . EM

Full Waveform Inversion . . . . . FWI

Frequency Domain Electromagnetic Methods . . . . . FTEM

Stretched Exponential . . . . . SE

Three-Dimensional 3D

Time Domain Electromagnetic Methods . . . . . TDEM

ACKNOWLEDGMENTS

I would like to take this as an opportunity to express my gratitude to the people who supported and guided me. This project would never have succeeded without them.

First of all, I would like to express my sincere gratitude to my advisor Dr. Andrei Swidinsky for the continuous support of study and research, for his motivation, knowledge, and patience. As a researcher, advisor, mentor, and friend, he has set an example of excellence. Also, many thanks to Dr. Seogi Kang for his time and the valuable conversations.

Next, thank you to the Ministry of National Education, Turkey, for the financial sponsorship for my M.S. I also would like to thanks my committee members Dr. Yaoguo Li and Dr. Rich Krahenbuhl. My dear friend Gurban Orujov and the many other graduate students always encourage and morally support me.

Finally, I would like to thank my family, who are always there for me. I would never have done this without their support.

In Memoriam of Mustafa Kemal Ataturk (1881 - 193∞)

CHAPTER 1

INTRODUCTION

1.1 Research Motivation

Direct current (DC) resistivity and induced polarization (IP) (Seigel, 1959) are used for determining the distribution of electrical conductivity and chargeability in the subsurface. As an essential tool in mineral exploration, IP surveys are commonly used to explore disseminated sulfide and/or porphyry deposits, which often have strong induced polarization responses. Some applications of IP have been successfully developed to determine the chargeable material in disseminated sulfide or porphyry deposits. (Pelton *et al.*, 1978). Also, some disseminated mineralization types are only sensitive to the IP method, and they show significant IP anomalies (Ward, 1990, Zonge *et al.*, 2005).

Applied geophysical methods are mostly used to explore for fossil fuels, ore minerals, groundwater, and geothermal reservoirs. In particular, electromagnetic methods (EM) are effective at imaging the fluid content of sedimentary rocks, as well as the presence of clay and certain electrically conductive minerals. In general, applying a time-domain electromagnetic (TDEM) survey can be done with a galvanic source or an inductive source. Electric field measurements with grounded electrodes called EIP surveys (Seigel, 1959).

Generally speaking, on a polarizable medium, a measured EM signal on a time-domain with a grounded source can be divided by three pieces depending on the time window. If one considers the signal measured after the current off, the early time of the signal will contain DC information, between the late time and the early time will be dominated by EM and the late time; the IP decay. However, there is a time window between the transition from EM to IP where two signals affect each other. In this specific time period, EM signals can contain some IP information, and/or IP signals can be blended with EM, and this is called EM/IP coupling. This effect is considered as noise in the traditional processing

and interpretation of IP data. This approach ignores the coupling between EM induction and IP and the relationship between time or frequency and IP relaxation. As a result, removing the coupling between EM and IP from grounded source surveys and increasing the sensitivity of IP phenomena become the primary focus in the mineral exploration industry and IP research. Similarly, in some works on airborne time-domain EM (ATEM) surveys, the primary attention is decoupling EM and recovering more IP information (Kang & Oldenburg, 2016). However, this EM signal may contain additional information about the subsurface's electrical properties. This blended signal can provide extra or maybe even better information about chargeability and conductivity.

In this thesis, the goal is to study and understand the effects, and importance of EM induction and how we can advantageously utilize it to collect more information from the subsurface. Since we have highly accurate numerical algorithms and computational power today, modern geophysical simulations can handle a large-scale three-dimensional (3D) DC/EM/IP modeling (Commer & Newman, 2004, Haber *et al.*, 2004). Furthermore, we can generate a grounded source DC/EM/IP data for a model with complex conductivity in the time domain (Marchant *et al.*, 2014) or simulate it in the frequency domain and can transform the results in the time domain (Hohmann & Newman, 1990). To simulate a full 3D grounded source DC/EM/IP survey, we have used a 3D simulation and parameter estimation package called SimPEG (Heagy *et al.*, 2017). This open-source python package allows us to generate a 3D geological model and simulate a grounded source time domainDC/EM/IP survey.

Originally, this project is started with a frequency domain approach using the Cole-Cole model. The Cole-Cole model is probably the most popular approach in terms of modeling complex conductivity. However, after a couple of months of work and lots of examples, we saw that this is very expensive because each response needs to be carried in the time domain with Fourier transform. In a 3D application with thousands of cells, this is quite challenging, time-consuming, and computationally expensive. Because of these reasons, we decided to use the SimPEG-EMIP (Kang & Oldenburg, 2016) package to simulate a model

with complex conductivity in the time domain by using the Stretched Exponential (SE) function. This method allowed us to simulate grounded source time domain DC/EM/IP data with a complex conductivity. Moreover, since all the calculation are done in the time domain, it is not necessary to carry out the results with Fourier transform. This method is not only computationally cheaper than a frequency domain approach but also lets us get the corresponding data in less time.

In application, we started with a realistic 3D porphyry model with complex conductivity to see the limits and the potentials of this method. This geological model with multiple units is originally used and presented by Kang & Oldenburg (2019). This model was slightly modified for use in the thesis. However, in the application, it was challenging to produce a pseudosection with the method developed, detailed in Chapter 2 and Chapter 3. These results led me to start with simpler geological models. Throughout this thesis, we modeled and simulated various types of geological models such as a conductive chargeable block buried in a resistive subsurface, a resistive chargeable block buried in a conductive subsurface, conductive chargeable block buried under a relatively resistive cover, and conductive chargeable block buried under a relatively conductive cover. By using these geoelectrical models in SimPEG and SimPEG-EMIP, we investigated the coupling between EM and IP. We aim to show that we can learn more about this dynamic phenomenon called IP and the coupling between EM and IP can provide extra conductivity and chargeability information than traditional DC/IP surveys by using the EM/IP coupling in grounded source time domain DC/EM/IP data.

1.2 Geophysical Background

Over the past 40 years, the DC/IP method has become a standard geophysical approach to collecting information about rock mineralogy and extensively used metal mineral exploration. First, in 1913, Conrad Schlumberger observed the IP effect (Seigel *et al.*, 2007) during their direct current experiments. For more than a decade, this effect did not get much attention due to technological limits. It was challenging to record and investigate this

signal. However, Schlumberger determined that the polarization effect occurs in the presence of mineralization. Later, this discovery caught the mining and petroleum exploration industry's attention. In the 1950s, the industry and researchers started to interest in the IP method to see its possibilities. In the mid-1950s, Soviet and American scientists investigated the chemical background of the polarization in lab experiments. Moreover, they made some successful and unsuccessful attempts to apply the method in mineral and petroleum explorations. This growing attention led to significant progress in instrumentation and their application (Zonge & Wynn, 1975).

On the theoretical side, Seigel (1959) introduced the mathematical equations of IP in the time domain for polarizable sphere and polarizable two-layer models. In the frequency domain, Collet *et al.* (1959) measured IP effects for frequencies with lab-scale experiments. Wait (1959) is also investigated the IP effect with lab and field works. With growing interest and knowledge of this geophysical method, DC/IP examined in mineral discrimination (Pelton *et al.*, 1978), spectral induced polarization and complex resistivity measurements (Pelton *et al.*, 1978, Zonge & Wynn, 1975), theory of borehole measuring of IP (Freedman & Vogiatzis, 1986), and hydrocarbon explorations (Oehler & Sternberg, 1982) Moreover, DC/IP method has been used in different fields such as environmental studies (Towle *et al.*, 1985), oil and gas exploration (Burtman *et al.*, 2014), archaeological investigations (Weller *et al.*, 2006) and in hydrogeology (Marshall & Madden, 1959). It is currently widely used for mineral exploration, geothermal and groundwater exploration, and environmental geophysical applications.

After 1980, the focus of interest has shifted to developing modeling and inversion methodologies in IP. Some publications such as Aiken *et al.* (1973), Fox *et al.* (1980), Guptasarma (1983), Oldenburg & Li (1994), Beard & Tripp (1995) and Li & Oldenburg (2000) show modeling and inversion techniques of induced polarization.

1.3 Thesis Outline

Chapter 1 starts with the research motivation of this work. Under the research motivation title, we explain the idea; would it be beneficial to use a signal that is generally considered noise in DC/IP surveys (EM/IP coupling) to extract more information about the subsurface with grounded source time-domain DC/EM/IP data with complex conductivity. Chapter 1 also gives brief information about the geophysical background and previous works on the IP method. The chapter ends with the thesis outline.

Chapter 2 gives a background information about induced polarization, measurement techniques, induced polarization theory, and its applications. Section 2.4, provides information about IP modeling techniques, time-domain method, stretched exponential, which is the time-domain approach that we have applied in simulating grounded source time-domain DC/EM/IP data, and why we chose to use this method. Chapter 2 also contains brief information about electromagnetic coupling and its types. These sections are followed by definitions of the governing equations, which are Maxwell's equations.

Chapter 3 starts with an overview of survey configurations, simulation times, and brief information about the computational side of this work. Then, we explain pseudoimpulse response of the electric field, which is the derivative of EM data with respect $\log_{10}$ time. This method was first introduced by Edwards (1997) and this amplitude independent response allows us to convert EM data to apparent resistivity (Equation 3.5). We also explain this response's sensitivity to σ, η, τ_{IP} and c. Chapter 3 shows all the simulation results of grounded source time-domain DC/EM/IP survey for various types of geological units. We start with a buried block as a simple geological model, and then we show the results of a conductive chargeable unit, resistive chargeable unit, and in the presence of the relatively resistive and relatively conductive cover. Finally, Chapter 3 presents the challenges faced with a geologically complex 3D porphyry-mineral model, and in the presence of a relatively resistive or relatively conductive cover.

Chapter 4 of the thesis describes the parametric inversion of grounded source time-domain DC/EM/IP data. We aim to recover model parameters using the Levenberg-Marquardt algorithm. This chapter demonstrates the possibility of recovering chargeability and conductivity information of the subsurface and the recovery of time parameters τ_{IP} and c of the model from the EM data. It gives brief information about the inversion methodology for grounded source time-domain DC/EM/IP data with stretched exponential: four parameters of a block embedded in halfspace inverted with the Levenberg-Marquardt algorithm. This example shows the possibilities and opportunities of EM and IP coupling, and these preliminary results may be used for developing a better workflow of 3D inversion of grounded source time-domain DC/EM/IP data with stretched exponential.

Chapter 5, which is the last chapter of this work, consists of three sections. These are conclusions, speculations and future works. Under these sections, we summarize the work, explain the results, and show possible paths for future research to expand this work.

CHAPTER 2
THEORETICAL BACKGROUND OF INDUCED POLARIZATION AND ELECTROMAGNETIC COUPLING

2.1 Introduction

In geophysics applications, a source and receivers are needed to generate data. The source is used to create a response from the material, and receivers measure the source's fields. Geophysical EM methods can be defined with the source type. In EM methods, the source can be natural as the magnetotelluric method or human-made, controlled. Natural source methods use natural electromagnetic fields in the atmosphere, and this method does not need an artificial source. Controlled source methods are used to measure the earth's response by generating currents from an artificial source. Generally speaking, there are two different types of controlled sources; grounded sources and inductive sources. In the case of grounded sources, the source and the earth need to be connected with wires and electrodes to inject the current to the ground and record the earth's response field. Two current electrodes are located in the ground. The current is injected by the positive electrode, and it returns to the negative electrode or sink electrode. Electric potentials generated by flowing galvanic currents through the earth can be measured at the surface. This grounded source survey is called the DC/IP survey. Figure 2.1 shows the different electrode configurations including the dipole-dipole array configuration that we use to simulate the grounded source time domain DC/EM/IP survey.

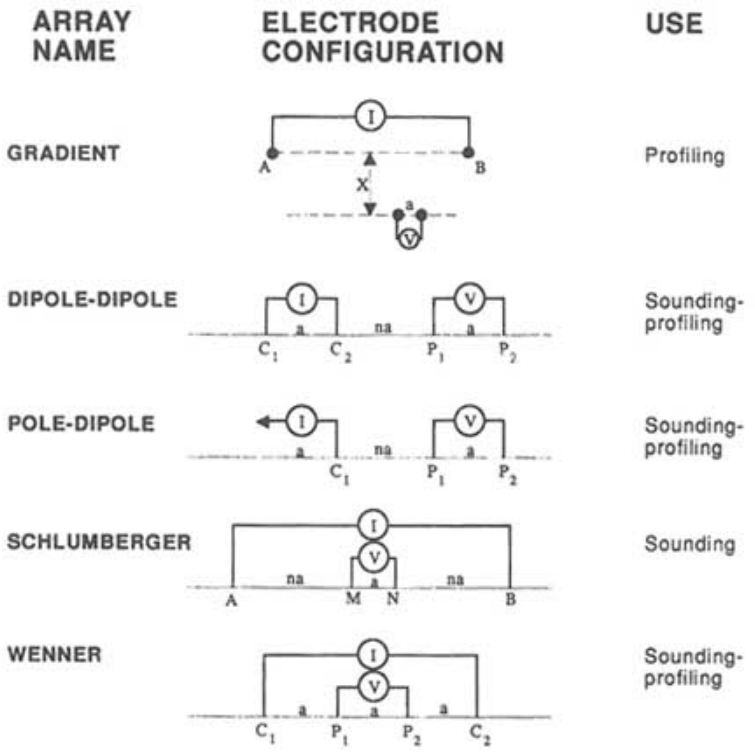

Figure 2.1: Various types of electrode configurations (Council, 1996). Two current electrodes A and B or C_1 and C_2 inject current to the ground and two measurement electrodes, M and N or P_1 and P_2 measure the potential different between electrodes.

An inductive source carries a time-varying current through a loop of wire. This time-varying current generates time-varying magnetic fields, and these fields act as the source fields. The conductive earth is induced by the field generated by the system and generates a secondary magnetic field. This field can be measured at the surface or above the surface (AEM). Both source types and their applications help us understand the physics of the earth's electromagnetic behavior. The source and the receiver type choice depends on the field operation. Galvanic and inductive sources both generate time-variant EM fields. However, some criteria such as field conditions, mobility of the system, and the moment of the transmitter should be taken into account in source selection. In this thesis, galvanic source type has been used in the method and its applications.

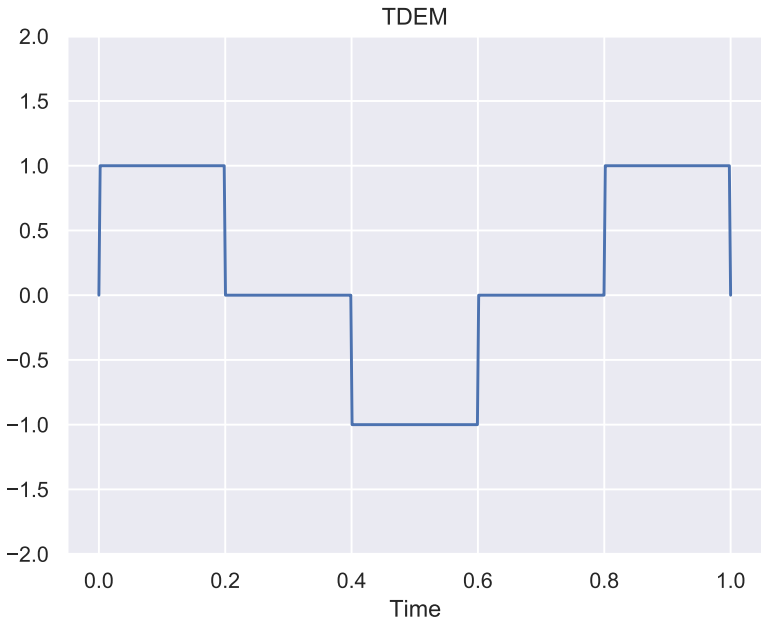

Figure 2.2: Step-off waveform with 50% duty cycle. Most TDEM and DC/IP systems use current with a specified duty cycle. The data is usually collected at the off-time.

The main idea behind these methods is to measure the electrical conductivity of the subsurface. However, the measurements can be affected by IP in the presence of chargeable geological units. The current generated from an artificial source flows into the conductive material. If this flow is blocked between two areas with different conductivities, these regions will act as capacitors, and charges will increase. Ideally, when the current source is turned off, these chargeable materials get discharged, and the subsurface returns to a natural state. This discharge occurs fast, and it is hard to determine this effect in a geophysical survey. However, some geological units show a larger polarization effect. In this case, these geological materials will be charged and discharged slowly in a finite, measurable time, and it can be observed in an EM survey. This is called IP, and this phenomenon can be defined as a delay in the subsurface's voltage response.

2.2 Induced Polarization Method

The IP method examines the polarization effect of the subsurface units that causes slow decay of the voltage for a certain period of time after the injected current cut off. With

this method, both the resistivity and polarization properties of the underground can be determined. The disturbance of the equilibrium states of the ions in the rock is responsible for the decay after the current cut.

In traditional DC/IP surveys, conventional electrical resistivity electrodes are used for IP measurements. These are two current and two non-polarizable potential electrodes. In application, when the current is switched off, materials in the ground will perform like a capacitor, and they will store the charge temporarily. Because of this chargeable behavior of the materials, the voltage between the potential electrodes will take time between seconds to several minutes to decay to zero.

2.2.1 Polarization Types

The source of underground physicochemical reactions that causes polarization is called electrode polarization in metallic minerals and membrane polarization in clay minerals. Electric current applied to the earth is carried by ions in the pores in the rocks. If metallic particles block the ions in the pore, they start to accumulate at the mineral boundary. After the current cut, the ions return to their equilibrium state. This movement of ions causes the effect of electrode polarization. Electrode polarization is often seen in metallic deposit areas. The magnitude of electrode polarization depends on some factors such as the current, the liquid content of the rocks and the pore structure, and the mineral concentration. A higher polarization effect can be seen on the disseminated mineral zones since the electrode polarization effect occurs on the mineral surface.

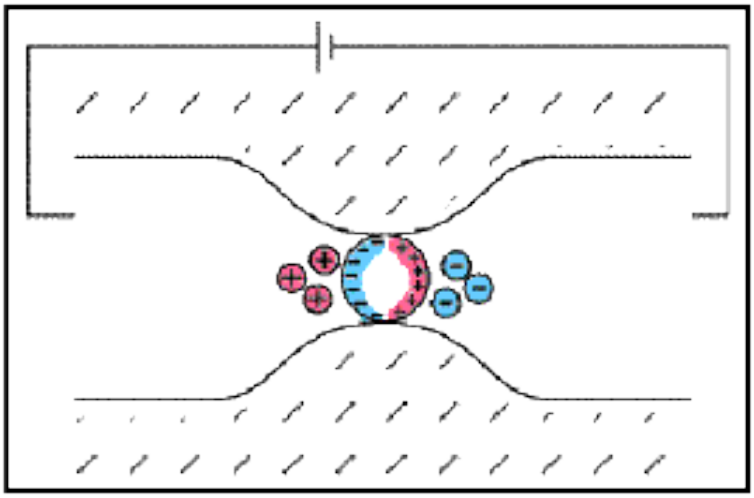

(a)

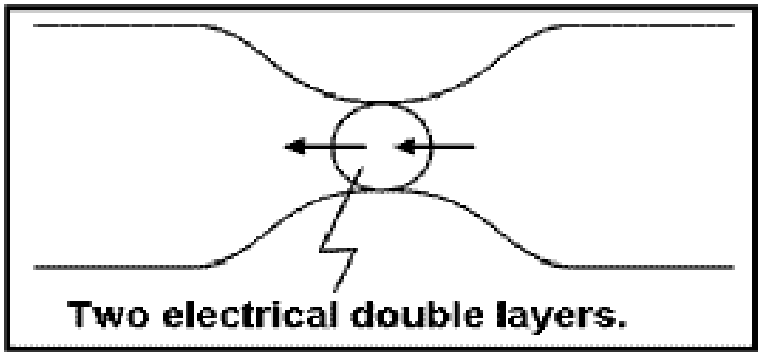

(b)

Figure 2.3: Electrode polarization. (a) With an applied electric field, when the pores of the mineral blocked by metallic particles, charges start to accumulate. (b) The accumulation causes a polarization and measured voltage at surface is affected by this phenomena. From gpg.geosci.xyz

Clay particles in the rock are charged with negative ions. Therefore, an ion cloud of positive ions is formed on them. When current is applied to the earth, this ion cloud and the ions are directed to the opposite side of the direction of the charge. When the current is applied to the ground cut, all ions return to their former positions. This ionic mobility observed in the presence of clay mineral underground causes the earth to polarize. This type of polarization is known as membrane polarization, and it occurs in porous sedimentary rocks, as shown in Figure 2.4. Such parameters, the pore ratio of the rock and its clay

content, and the clay distribution affect the polarization magnitude.

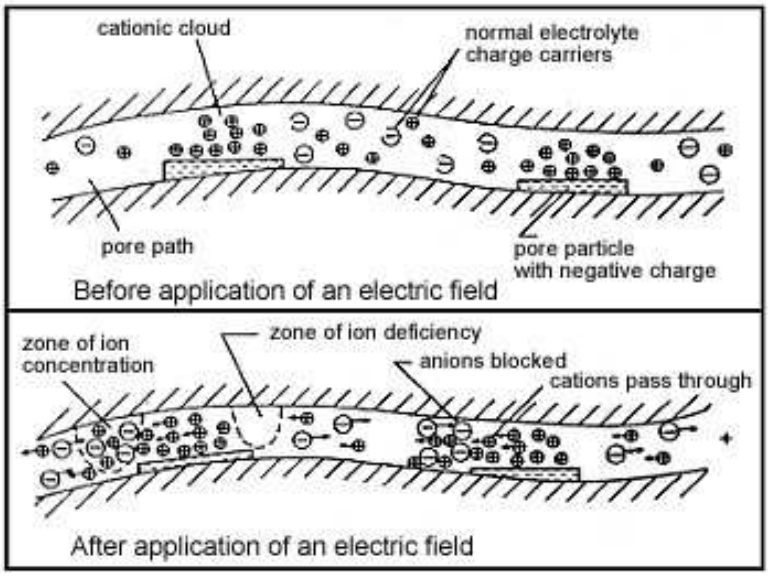

Figure 2.4: Membrane polarization in a rock with clay content (Ward, 1990).

2.3 Time Domain IP Method

The field application of the DC/IP method can be operated in both the time-domain and the frequency-domain. In time-domain applications, zero frequency current (direct current) is used, while the frequenct can be varied between high and low-frequency in the frequency-domain. This work is based on the time-domain approach. More information about the frequency-domain IP method can be found in Bertin & Loeb (1976) and Sumner (1976).

In time-domain measurements, measured voltage does not fall to zero and instead, decreases for a certain period of time after the applied current cut. With the processing of this decay curve, chargeability (η) can be observed. The IP effect parameter is obtained from the voltage difference ratio when the direct current is applied and the voltage difference when the current is cut.

In Figure 2.5, V_m is the potential when polarization charge is at maximum, V_σ is the potential measured in the absence of chargeability, and V_s is secondary potential or, the decaying potential, can be observed after the current cut. The red area can be defined as a

decay curve, and the integration of this decay curve can obtain chargeability.

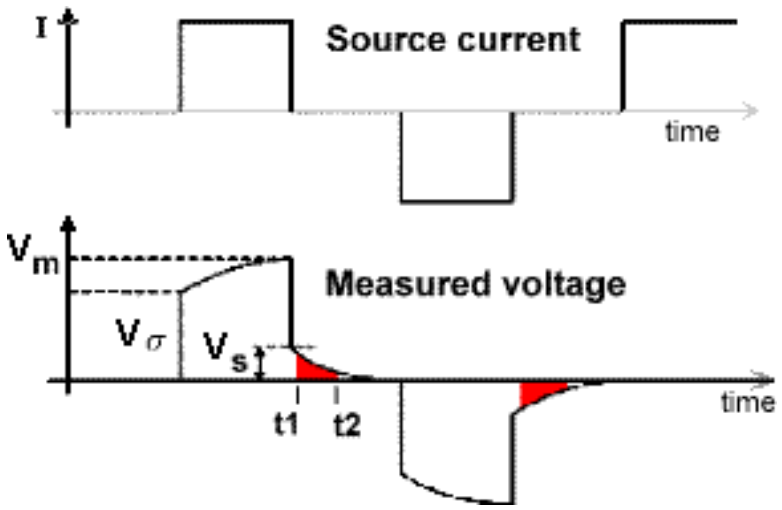

Figure 2.5: Applied current, measured voltage relationship and relaxation curve in time domain measurements. From www.eoas.ubc.ca

$$\eta = \frac{1}{V_m} \int_{t_1}^{t_2} V_s(t) dt \tag{2.1}$$

In time-domain IP measurements, measured polarization parameters can be affected by some variables such as applied current (I), current injection start and end time, sampling time, or the device parameters. Modern devices are controlled by computers, and it is easy to define and change these parameters. However, since these parameters directly affect measured values, it is essential to decide and test them beforehand. The current apply time is also equally crucial in time domain IP measurements. If the applied time is not long enough, the subsurface materials cannot be polarized, which causes not to see the IP effect correctly.

IP measurements are done with non-polarized electrodes. This is because if the electrodes can be polarized, they build charges on themselves under the applied current. Also, telluric currents cause noises in IP measurements. Since the telluric currents have a large period, measured and relaxation times can be reduced to reduce the noise level in IP measurements. However, in this case, enough time period for the polarization can be a problem (Bertin &

Loeb, 1976).

2.4 Modeling IP

IP is a powerful tool in mineral exploration, especially in ore bodies, since it is directly related to metallic grains (Revil *et al.*, 2015). IP method can experiment in both the frequency domain and the time domain. When we model the IP effect, we are interested in Ohm's law, which describes the relationship between voltage (V), electric current *(I)*, and resistance (R). Ohm's law defined the current flow in the absence of IP when an electric field applied;

$$\vec{J} = \sigma \vec{E} \tag{2.2}$$

where sigma is electrical conductivity (S/m). However, some subsurface materials are chargeable, and those materials can act as capacitors and store charge. In the presence of IP, the standard Ohm's law needs to be modified to model these IP effects. This phenomenon characterized by Seigel (Seigel, 1959) by introducing the chargeability to Ohm's law;

$$\vec{J} = \sigma(1-\eta)\vec{E} \tag{2.3}$$

where η is called chargeability, a unitless number between [0,1). η describes the polarization magnitude, and it allows us to interpret the standard time-domain IP effect caused by the accumulated charge in a finite time. Some experts have shown that IP characteristic is an excellent indicator to determine different mineral types with similar chargeabilities and conductivities (Pelton *et al.*, 1978, Van Voorhis *et al.*, 1973, Zonge *et al.*, 2005). These materials show different IP results as a function of frequency. The most common model that is used is the Cole-Cole model. This model is originally defined by Cole and Cole (Cole & Cole, 1941), and Pelton (Pelton *et al.*, 1978) has shown laboratory results that successfully segregate different mineral types with the Cole-Cole formulation. Since than, the Cole-Cole model has become a standard approach for IP spectrum analysis for minerals.

Moreover, as an alternative, Zhdanov (Zhdanov, 2008) suggested an IP model based on an effective medium theory called GEMTIP and showed that Cole-Cole formulation could be analytically derived from GEMTIP.

Practitioners and researchers do not model EM's full nature in the spectral and standard IP data processing. EM induction effects are considered as noise in such interpretations. This induction effect is called EM coupling. In the traditional approach, survey design arranged to minimize the EM coupling or EM coupling removed from data in the data processing step (Routh & Oldenburg, 2001). Some authors such as Kang & Oldenburg (2016), Smith (2016) have worked on decoupling IP and EM effects in ATEM to increase the awareness of pure IP signal. However, the coupling between EM and IP can be advantageous, and this coupling can contain additional IP information about the interested geological model. The coupling between EM and IP needs to be modeled with a complex conductivity model to achieve this task. The Cole-Cole model is the most popular approach for such cases. The problem with modeling an IP response in the time domain by using the Cole-Cole model is computationally expensive. Since the Cole-Cole model is defined in the frequency domain, we need to convert all the responses to the time domain with a Fourier transform. Recently, some publications (Belliveau & Haber, 2018, Kang & Oldenburg, 2019) proposed a parametrization to model a complex resistivity in the time domain, called Stretched Exponential (SE) function.

2.4.1 Cole-Cole Model

In the frequency-domain, frequency dependent behaviour of conductivity defines IP. This is also described as low frequency dispersion of the conductivity. In 1978, Pelton translated this into a complex conductivity model by using Ohm's law (Pelton *et al.*, 1978). This model is called the Cole-Cole conductivity model;

$$\sigma(\omega) = \sigma_\infty - \frac{\sigma_\infty \eta}{1 + (1-\eta)(i\omega\tau)^c} \tag{2.4}$$

where $\omega = 2\pi f$ is the angular frequency, η is the chargeability, introduced by Seigel (Seigel, 1959), τ is the time constant of the decay which controls the relaxation, c frequency exponent, ranges from 0 to 1 (Pelton *et al.*, 1978) describes the frequency dependence, and governs the shape of the spectrum.

This model became the most commonly used approach, often used in practical applications and fit experimental data. However, this method can be computationally expensive. In particular, since each regular grid value in discretization needs to be carried out to the time-domain with a Fourier transform, 3D simulations with this model are computationally intensive and expensive.

Originally, this work started with a frequency domain approach using the Cole-Cole model. However, this method is highly expensive and time-consuming. We started to search for an alternative or, better, another model that we can directly simulate in the time-domain. This led us to experiment and use a stretched exponential approach to simulate grounded source time-domain DC/EM/IP data with complex conductivity.

2.4.2 Stretched Exponential Function

The Cole-Cole model has been used to define and model complex resistivity for decades. However, the implementation of the Cole-Cole model for the time domain is computationally expensive because calculations need to be transformed to the time domain from the frequency domain by Fourier transform. Especially when working on a 3D model it becomes more computationally intensive and expensive since the number of cells for discretization dramatically increases. Recently, Kang & Oldenburg (2019) have shown a new approach to describe and model the IP decays in the time domain called the stretched exponential model. This technique's main advantage is being computationally cheaper than carrying out the required Fourier transform from the frequency-domain to the time-domain for each time step. This advantage is crucial, especially when working on 3D modeling and simulation. Similarly, Belliveau & Haber (2018) have also simulated IP decays on time-domain with SE function. There are three main differences between the two publications. First, Kang &

Oldenburg (2019) have obtained an impulse conductivity function in the time domain by using the SE function, whereas Belliveau & Haber (2018) have defined an ordinary differential equation which is converted from Ohm's law with the SE function. Secondly, two publishers have used different Cole-Cole models. Kang & Oldenburg (2019) have used the model explained in Tarasov & Titov (2013). On the other hand, Belliveau & Haber (2018) have developed their approach based on a Cole-Cole model from Pelton *et al.* (1978). Finally, their definition of SE function is different. Kang & Oldenburg (2019) have defined the SE function as (Kohlrausch, 1854):

$$f(t) = exp\Big(- \Big(\frac{t}{\tau_{se}}\Big)^{c_{se}}\Big) \tag{2.5}$$

whereas Belliveau & Haber (2018) have used:

$$f(t) = exp\Big(- \frac{t^{\beta}}{\tau}\Big) \tag{2.6}$$

Since we have used an open-source Python package is called SimPEG-EMIP (Kang & Oldenburg, 2016), application in this thesis based on their SE function preference and their IP decay modeling approach. They have shown that for a period of time, their SE model converges well with the Cole-Cole model, as regards the relationship between Cole-Cole and SE parameters. However, SE and the Cole-Cole model are not completely the same and it is not possible to fit the entire Cole-Cole model with a single stretched exponential. They show very similar time-features, and the two models are equal when $c_{cc} = 1$ which is called the Debye model (Debye, 1929).

Kang & Oldenburg (2019) have shown how to parameterize the SE function and define a step-off conductivity response. Equation 2.5 defines the time domain SE function, and this equation can be used to describe the step-off response in the time domain:

$$\sigma_{se}^{step-off} = \sigma_{se} \circledast (1 - u^{step-on}) \tag{2.7}$$

where subscript se defines SE, $u^{step-on}(t)$ is the Heaviside step function, and $\circledast$ is convolution operator. For example, $f \circledast g$ can be written as:

$$f \circledast g = \int_{-\infty}^{\infty} f(u)g(t-u)du \tag{2.8}$$

When $t \leq 0$, Equation 2.7 will be:

$$\sigma_{se}^{step-off} = \sigma_{\infty}(1-\eta_{se}) \tag{2.9}$$

and when $t > 0$, Equation 2.7 can be defined as:

$$\sigma_{se}^{step-off} = -\sigma_{\infty}\eta_{se}exp\Big(-\Big(\frac{t}{\tau_{se}}\Big)^{c_{se}}\Big) \tag{2.10}$$

To compute IP response in the time domain, we need a linear IP equation. This equation can be derived by taking the derivative of $\sigma_{step-off}$ with respect to time and multiplying the result by -1. The result will be σ_{se} or the SE conductivity. The result can be regarded as an impulse response and can be defined as:

$$\sigma_{se}(t) = \sigma_{\infty}\delta(t) - \sigma_{\infty}\eta_{se}t^{-1}\Big(\frac{t}{\tau_{se}}\Big)^{c_{se}}exp\Big(-\Big(\frac{t}{\tau_{se}}\Big)^{c_{se}}\Big) \tag{2.11}$$

where $\delta(t)$ is the Dirac-Delta function. Equation 2.11 shows that σ_{se} or SE conductivity has a definition in time domain. With this definition, we do not need to carry out a Fouirer transform for $\sigma(\omega)$ to obtain $\sigma(t)$ within value of each regular grid in discretization.

2.4.3 Comparison of The Impulse Responses of Cole-Cole and Stretched Exponential

In this section, we compare the time domain response of the Cole-Cole model and the stretched exponential function. The original expression in geophysical applications was introduced by Pelton *et al.* (1978). Tarasov & Titov (2013) also proposed a definition of the Cole-Cole model with slight differences. There are still debates on the definitions and the differences between equations (Kozhevnikov & Antonov, 2021, Macnae, 2015).

Marchant (2015) showed how to obtain time domain impulse response of Pelton's Cole Cole definition with applying an inverse Laplace transform. We will follow the inverse Laplace transform approach for Tarasov & Titov (2013) definition of the Cole-Cole model. This model can be defined as,

$$\sigma(\omega) = \sigma_\infty - \frac{\eta\sigma_\infty}{1 + (i\omega\tau)^c} \tag{2.12}$$

When c=1, this frequency dependent conductivity is called the Debye model. This equation can be rearranged,

$$\sigma(\omega) = \sigma_\infty - \frac{\sigma_\infty\eta}{\tau}\frac{1}{\frac{1}{\tau} + i\omega} \tag{2.13}$$

We can apply an inverse Laplace transform (Abramowitz & Stegun, 1964),

$$\mathcal{L}^{-1}\left[\frac{1}{a+s}\right] = e^{-at}u(t) \tag{2.14}$$

after the inverse Laplace transform, the Debye model in time domain can be defined as

$$\sigma(t) = \sigma_\infty\delta(t) - \frac{\sigma_\infty\eta}{\tau}e^{-\frac{t}{\tau}}u(t) \tag{2.15}$$

When c = 1, Debye and SE models are equal, and both models show the same characteristic in the time domain. I compared the impulse response of the Cole-Cole model and the impulse response of the stretched exponential and plotted the result in Figure 2.6. On the other hand, Pelton *et al.* (1978) also showed the expressions in the time domain. Pelton *et al.* (1978) Equation 5 shows the general time domain expression, and Equation 4 is the simplified version of Equation 5 when c = 1. Hilfer (2002) is the only paper that investigates the different relaxation models and shows the time series definition of those relaxation models. This publication also shows that CC and SE are equal when c = 1. Moreover, this publication can provide a better insight into the time domain definition of Pelton *et al.* (1978) Equation 5. However, while SE and CC impulse responses are equal when c = 1, the

Figure 2.6 shows that they are not equal to Pelton *et al.* (1978) definition. In Figure 2.6, for c = 1, both equations from Pelton *et al.* (1978) matches. Since we use Tarasov & Titov (2013) definition of the CC model, they do not match perfectly. The other reason could be the difference in the definition of chargeability in both publications.

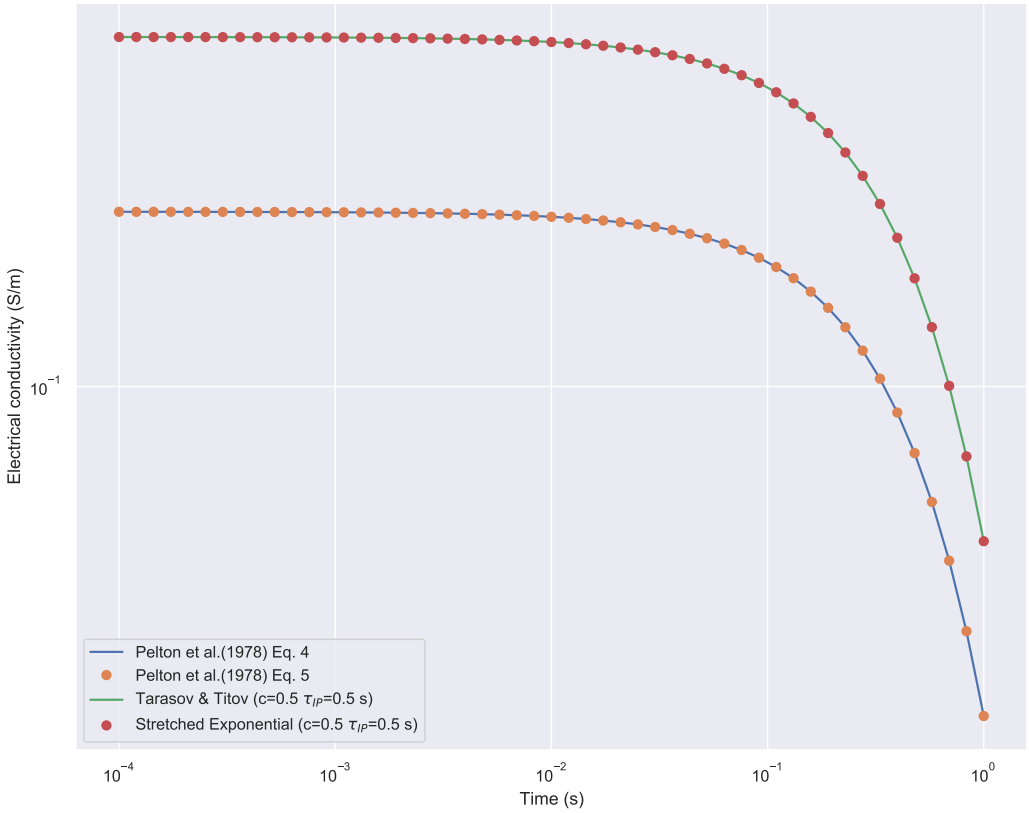

Figure 2.6: SE impulse response vs Cole Cole impulse response in time domain. For both models, $\sigma = 1$ S/m, $\eta = 0.2$ V/V, $\tau = 0.1$ s, and c = 1.

Similarly, we can follow the same for c = 0.5. Taking the inverse Laplace transform (Abramowitz & Stegun, 1964)

$$\mathcal{L}^{-1}\left[\frac{1}{a+\sqrt{s}}\right] = \left(\frac{1}{\sqrt{\pi t}} - ae^{a^2 t}\text{erfc}(a\sqrt{t})\right)u(t) \tag{2.16}$$

For c = 0.5, time domain impulse response of the Cole-Cole model become

$$\sigma(t) = \sigma_\infty \delta(t) - \sigma_\infty \eta b \left(\frac{1}{\sqrt{\pi t}} - b e^{a^2 t} \mathrm{erfc}(b\sqrt{t}) \right) u(t) \tag{2.17}$$

where b = $\frac{1}{\sqrt{\tau}}$.

When c is not equal to 1, the two complex conductivity models are not equal. Moreover, as mentioned in the previous subsection, it is not possible to fit CC with a single SE function. Here, we examined this and fixed $\sigma = 1$ S/m, $\eta = 0.2$ V/V, and only for CC, we fixed c= 0.5. We used a least squares algorithm to find τ_{IP} and c values for SE.

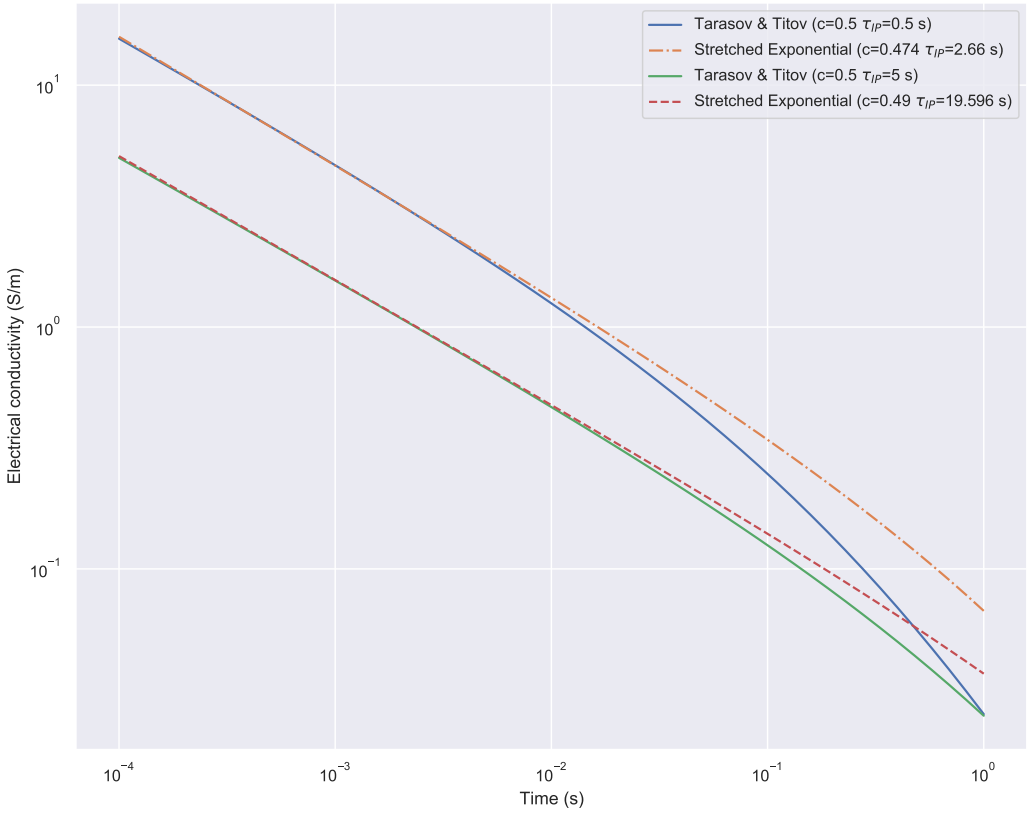

Figure 2.7: SE impulse response vs CC impulse response in time domain for c = 0.5. For both models, $\sigma = 1$ S/m and $\eta = 0.2$ V/V. For CC, c fixed to 0.5.

Table 2.1: Comparison of resultant SE parameters and the CC parameters.

	CC	SE	CC	SE
σ (S/m)	1	1	1	1
η (V/V)	0.2	0.2	0.2	0.2
τ_{IP} (s)	0.5	2.66	5	19.596
c	0.5	0.474	0.5	0.49

Table 2.1 shows the parameters of CC and SE curves in Figure 2.7. Results show that mostly early time and mid time data fit better. They still show the same time characteristic, and also they fit in a certain time period. Even if the c values are close to each other, differences in τ_{IP} can be large.

Since it is not possible to transform analytically when c is different than 0.5 and 1, CC impulse responses in time domain when c = 0.4 and c = 0.6 transformed numerically with the python implementation of the inverse laplace transform with Gaver-Stehfest algorithm (Gaver, 1966, Stehfest, 1970a,b). Here, τ_{IP} fixed 0.5 s, σ = 1 S/m, η = 0.2 V/V. The numerical algorithm compared to analytical inverse Laplace transform in Figure 2.8. The same least squares curve fit routine used to obtain c and τ_{IP} values of SE impulse response. Figure 2.9 shows the comparison of the impulse responses of CC and SE in time domain. Again, we can see the similarity between the two models. However, still not possible to fit them with the same parameters.

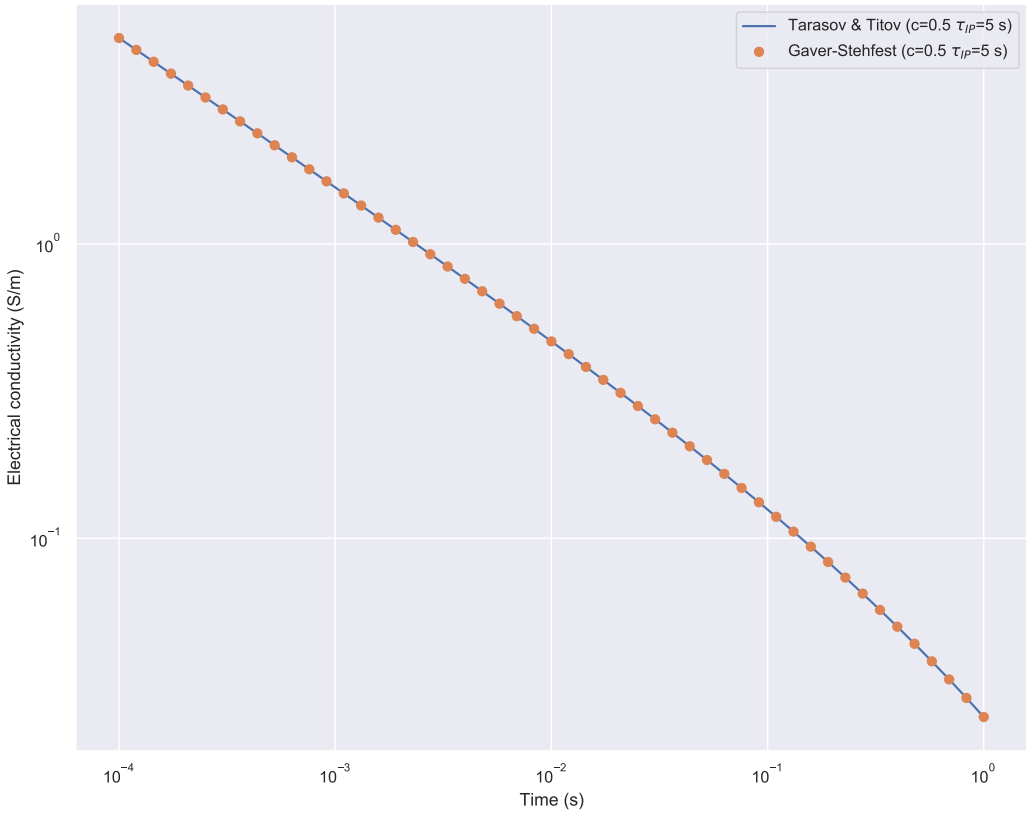

Figure 2.8: Time domain impulse responses of analytical (CC) and the numerical (Gaver-Stehfest) results. σ fixed to 1 S/m and η fixed to 0.2 V/V.

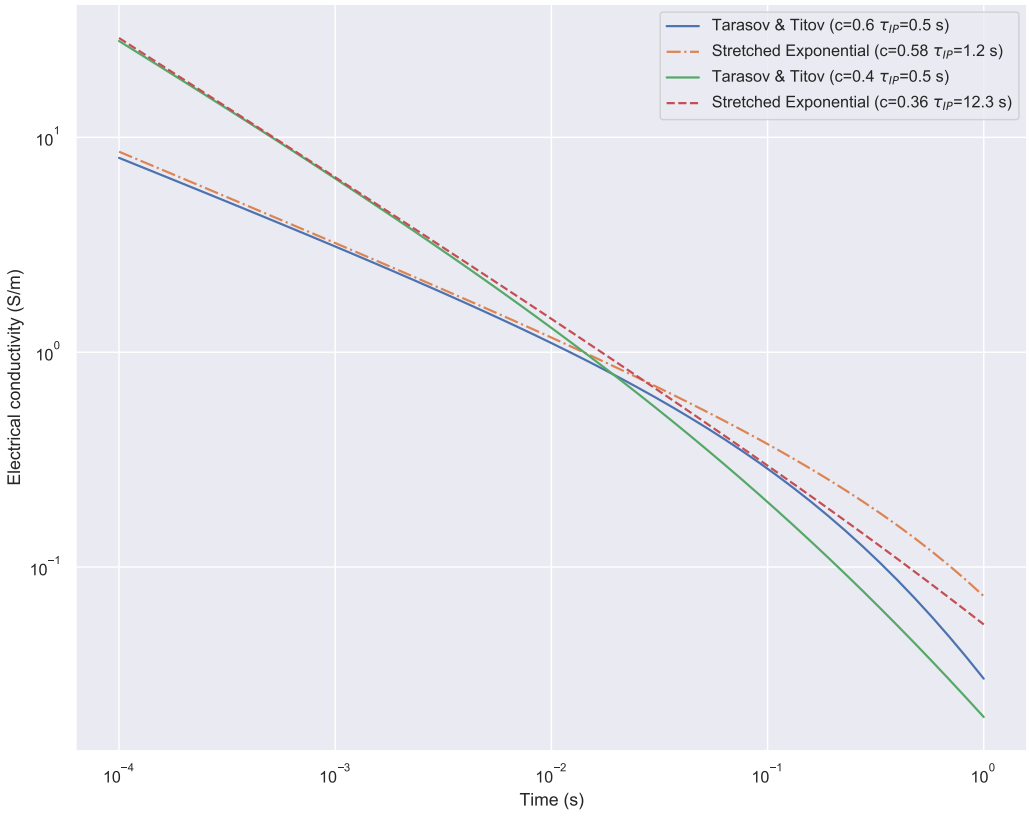

Figure 2.9: SE impulse response vs CC impulse response in time domain for c = 0.4 and c = 0.6. τ_{IP} and c values of SE impulse response obtained from least square routine.

2.5 EM Coupling in IP

On early IP applications, the practitioners have identified an exciting behavior; IP response distorted by EM effect between the source and the receiver (Wait, 1959). The measured potential at the receiver contains EM coupling between the source and receiver. Such factors as the used source waveform, the array's geometry, and the subsurface's resistivity model make EM coupling a complex function.

IP source and the receivers can act as an electrical transformer in some conditions and, the primary field induces a secondary field due to the electrical induction effect. This induction effect of EM coupling generates responses that are similar to IP responses. However, these effects are not caused by any natural polarization like IP.

The idea of EM coupling is first represented by Ward (1967). In IP, the term coupling points out three different EM phenomena between the relationship of the IP receiver and the transmitter. Resistive coupling is simply the measured resistivity of the ground, respect to transmitter and receiver locations. An applied current will cause a potential difference between the source electrodes and the receivers. This difference is divided by the applied current and multiplied by the array arrangement's geometric factor. The result will be an apparent resistivity.

Capacitive coupling appears when a voltage change is caused by a displacement current or electrical leakage between the source and the receiver wires, source, and earth. This type of coupling can be avoided by keeping wires separated and reducing the contact impedances at the electrodes (Wait, 1959).

Inductive coupling can be defined as a frequency-dependent mutual inductive impedance of two grounded wires. In infinite wires, this impedance can be calculated in a non-conductive, homogeneous whole space. However, this coupling becomes a complicated problem when the wires have a finite length as we use in real life IP measurements, more complex geology, and a half-space with conductive materials.

2.6 Maxwell's Equations

Maxwell's equations govern the physics of EM. The behavior of EM fields can be described by a set of partial differential equations (PDEs) in the frequency-domain or in the time-domain. In the time-domain, Maxwell's equations:

$$\nabla \times \vec{e} = -\frac{\partial \vec{b}}{\partial t} \tag{2.18}$$

$$\nabla \times \vec{h} - \vec{j} = \frac{\partial \vec{d}}{\partial t} \tag{2.19}$$

where $\vec{e}$ is the electric field (V/m), $\vec{b}$ is the magnetic flux density (T). $\vec{h}$ is the magnetic field (A/m), $\vec{d}$ is the electric displacement (C/m^2) and $\vec{j}$ is the electric current density (A/m^2). Equation 2.18 describes that if a magnetic flux changes by time, this will generate an electric field—this equation is called Faraday's law. Equation 2.19 known as the Ampere-Maxwell equation, and it describes that the current creates magnetic fields.

Maxwell's equations can also be expressed in the frequency domain. In order to define the equations in the frequency-domain, the Fourier transform can be used;

$$F(\omega) = \int_{-\infty}^{\infty} f(t) e^{-i\omega t} dt \tag{2.20}$$

$$f(t) = \frac{1}{2\pi} \int_{-\infty}^{\infty} F(\omega) e^{i\omega t} d\omega \tag{2.21}$$

where upper case letters represent the frequency-domain, and lowercase letters represent the time-domain. Maxwell's equations in the frequency-domain can be obtained with Fourier transform, and these equations are given by;

$$\nabla \times \vec{E} = -i\omega \vec{B} \tag{2.22}$$

$$\nabla \times \vec{H} - \vec{J} = i\omega \vec{D} \tag{2.23}$$

where Equation 2.22 is Faraday's law in frequency domain and Equation 2.23 Ampere-Maxwell equation in frequency domain. Also, the EM character of most materials can be

defined by the constitutive relations;

$$\vec{J} = \sigma\vec{E} \tag{2.24}$$
$$\vec{B} = \mu\vec{H} \tag{2.25}$$
$$\vec{D} = \epsilon\vec{E} \tag{2.26}$$

where σ is electrical conductivity (S/m), μ is magnetic permeability (H/m), and ϵ is the dielectric permittivity (F/m). Also, resistivity is the reciprocal of electric conductivity has units of Ωm.

$$\rho = 1/\sigma \tag{2.27}$$

As a physical property, conductivity depends on the material type. For example, the conductivity of air is 10^{-8} S/m, and gold has a conductivity of 4x10^{7} S/m. Magnetic permeability characterizes the strength of induced magnetism, a material caused by an external magnetic field and the free space magnetic permeability, mostly used as the value of magnetic permeability ($4\pi \times 10^{-7}$ H/m). Similarly, for most materials, the order of the dielectric permittivity of free space can be used (8.85×10^{-12} F/m).

CHAPTER 3

NUMERICAL EXAMPLES AND SIMULATION RESULTS

3.1 Introduction

This section shows the forward simulation results of grounded source TDEM data. For each simulation result, we plotted DC and DC/EM/IP pseudosections, and compared the subsurface images. The fundamental idea behind this comparison is one method does not contain the EM and IP coupling and shows the t=0 response (DC), where the other one uses the entire EM signal (DC/EM/IP). Simply, in each section, we compared Equation 3.1 results with Equation 3.5 results of grounded source time-domain DC/EM/IP data.

The traditional DC imaging technique does not take EM and IP coupling into account. Moreover, this signal is generally considered as noise. Using a full EM signal which contains the Earth's inductive response, we generated DC/EM/IP pseudosections. This method contains coupling between EM and IP. Like a full waveform inversion (FWI) in seismic methods, this technique uses the full EM response for a better understanding about this coupling. Extracted information and knowledge from this method may help to generate a better subsurface image with EM tomography in future projects.

3.1.1 DC Response

DC calculations have been done by converting the recorded E_x field at t=0 to ρ_{app}. In order to do this, first we calculated potential V from E_x, then we used the converted V on dipole-dipole apparent resistivity formula;

$$\rho_{app} = \frac{\Delta V}{I} \pi n a (n+1)(n+2) \tag{3.1}$$

where a is electrode separation and n is an integer. The main reason for calculating and generating pseudosections from ρ_{app} is data reduction.

Similarly, for the sake of data reduction, we can also calculate η_{app} which is the apparent chargeability. This is also called the overvoltage effect.

$$\eta_{app} = \frac{V_{\text{late}} - V_{\text{early}}}{V_{\text{late}}} \tag{3.2}$$

Throughout this work, we were only interested in the DC response, so we calculated Equation 3.1 and imaged ρ_{app} response for DC pseudosections.

3.1.2 Pseudoimpulse Response of the Electric Field

In a typical TDEM survey, the step response of the system is the measured electric field. This can be done by switching on or off the TX abruptly. To convert this recorded step response into the impulse response, we need to take the derivative of the data with respect to time. As an alternative, Edwards (1997) suggested a newly derived measurement called pseudoimpulse response, which can be obtained by taking the derivative of the data with respect to logarithmic time. This method can be used for any step-on or step-off response. This allows us to find the peak arrival time of the signal for each source and receivers pairs and we can calculate the ρ_{app} with this arrival time. The reason for using this technique is data reduction and to simplify the analysis.

The fundamental differential equation for diffusion equation, which is the time-dependent EM fields in a conductive media can be written as;

$$\nabla^2 E = \mu\sigma \frac{\partial E}{\partial t} \tag{3.3}$$

where E is electric field (V/m), σ is the conductivity (S/m) and μ is magnetic permeability (H/m). Swidinsky *et al.* (2015) have shown a dimensional analysis for Equation 3.3

$$\frac{1}{[\text{lengthscale}]^2} = \frac{\mu\sigma}{[\text{timescale}]} \tag{3.4}$$

and they have also converted this analysis into an equation;

$$\tau_{EM} = \frac{\mu\sigma r^2}{b} \tag{3.5}$$

where τ_{EM} is a characteristic time of the field.

We can use this method for each source and receiver pair and take the logarithmic time derivative of the calculated electric field. Each normalized pseudoimpulse response curve will show a unique characteristic, which depends on the subsurface's geoelectrical model. As we can see in Figure 3.1, so-called peak arrival times, similar to the seismic method - a shot gather. If we treat this arrival time curve as seismic shot gathers, we can see that the peak arrival time we are interested in gets bigger with offset. In Equation A.3, τ_{EM} is the time of this maximum point. After obtaining τ_{EM}, we can calculate an apparent resistivity response for each source and receiver pair, and it can be written as;

$$\rho_{app} = \frac{\mu r^2}{b\tau_{EM}} \tag{3.6}$$

In Equation 3.5 and Equation 3.6, b is a scaling constant and it can be between 6 and 16. In Appendix A, we extend this result and show how we have chosen b with analytically derived τ from Ward & Hohmann (1988) Equation 4.174.

Equation 3.6 is important because like Equation 3.1, we can calculate the ρ_{app}. The main difference between the two equations is, Equation 3.6 carries information from an entire EM signal. This is important because this signal contains EM and IP coupling and this amplitude independent response of the signal allows us to include this coupling when imaging the subsurface.

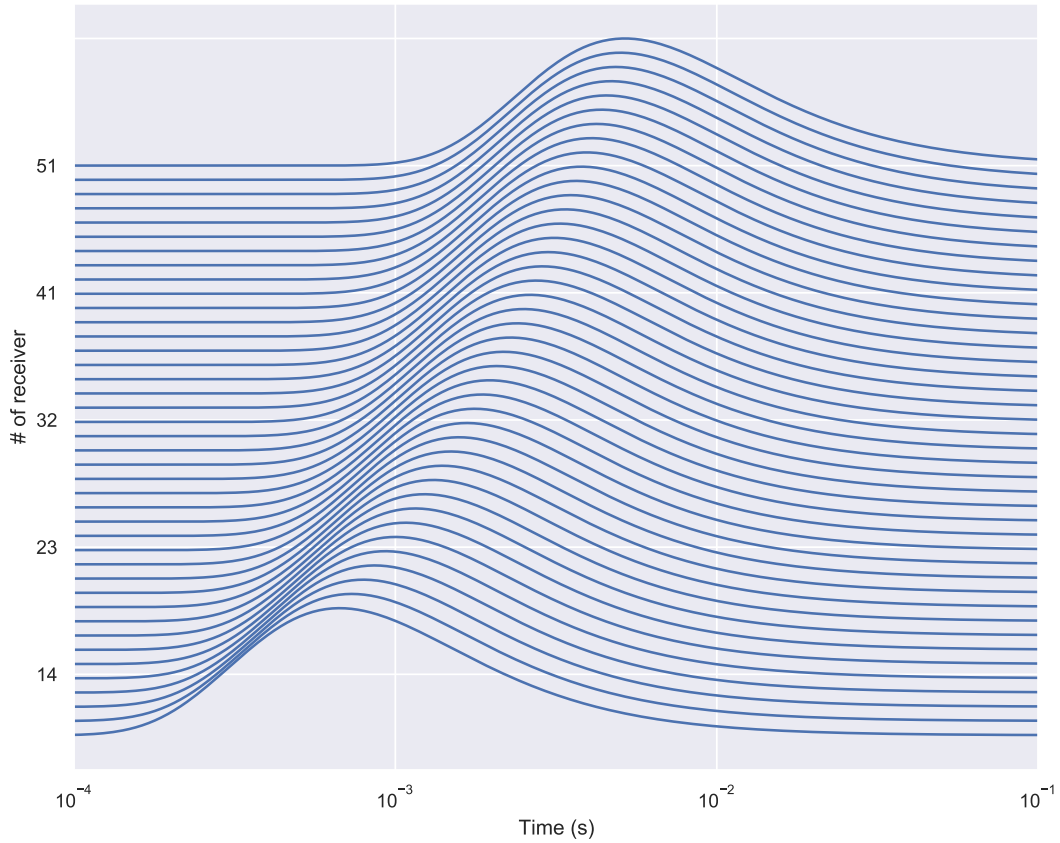

Figure 3.1: Pseudoimpulse Response of halfspace with $\sigma = 10$ S/m. Electric field has calculated with Ward & Hohmann (1988) Equation 4.174, then log_{10} time derivative calculated for each receiver response.

3.2 Modeling Details

DC responses are calculated with t=0 response of the field, since we used step-off waveform. For DC/EM/IP pseudosections, before calculating the log_{10} time derivative of the data, we filtered the results with the Savitzky & Golay filter (Savitzky & Golay, 1964). The Savitzky & Golay filter is a weighted sum of a finite number of data samples, and it is a low pass filter (smoother). This filter eliminates the small numerical errors in the data and generates a smoother response. Since we calculated the log_{10} time derivative of the data, the numerical errors became larger, and that caused spikes in normalized pseudoimpulse.

Since the simulations are computationally intensive, we used the Colorado School of Mines' cluster Mio. For the block model without a cover, each simulation takes approximately 52 hours, with 2x(Intel X5670) 12 Cores 2.93 GHz Cpu and 24 GB RAM configuration.

On the block model simulations, the simulated area has discretizated with SimPEG tensormesh with 171.304 cells. Figure 3.3 shows the mesh that we used for the grounded source DC/EM/IP simulations. In order to avoid the boundary effects, I extended the mesh with a padding of 8. The reason for this is reducing the numerical errors that can be caused or amplified by the boundaries.

The source is a dipole with 2 meters dipole distance. We used 51 receivers and the receivers are positioned from -250 meters to 250 meters with 10 meters distance. The first source position is -250 meters. After recording the electric field on the x direction (E_x) by all receivers, we moved the source with 10 meters until the last position, 250 meters. The recording time has 400 samples, logarithmically spaced from 10^{-5} seconds to 1 seconds.

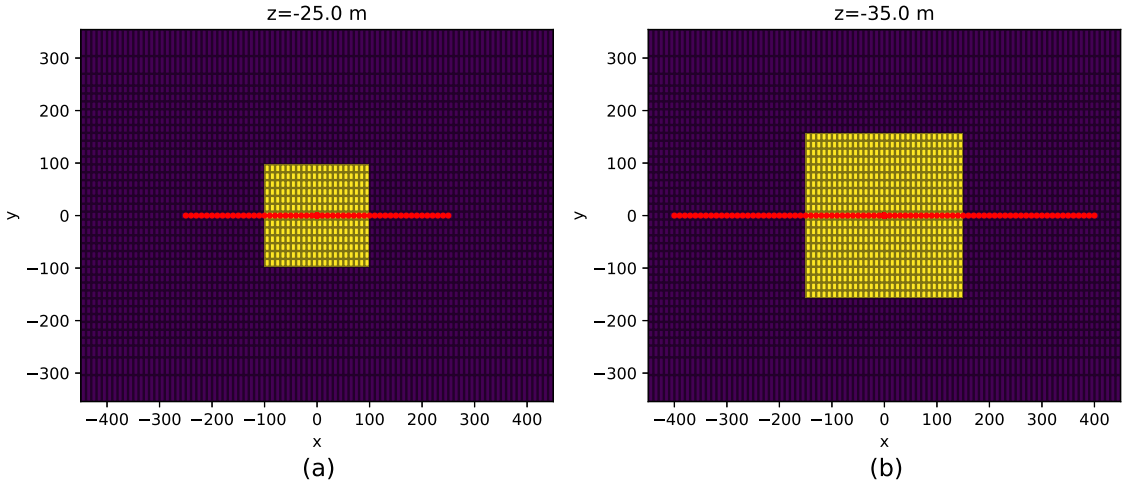

Figure 3.2: Plan map of the surveys. (a) Plan map of the simulations of a block. Red dots represent 51 receivers with 10 meters spacing. (b) Plan mat of the simulations of a block buried under a cover. Red dots represent 81 receivers with 10 meters spacing.

Where the block is under a relatively resistive or conductive cover, we used 81 receivers with 10 meters spacing to make the aperture larger. The source type and the dipole distance is the same with the block model simulations. We used SimPEG tensormesh for discretization with 238.924 cells. Since the survey area was larger in these cases, each simulation took approximately 98 hours.

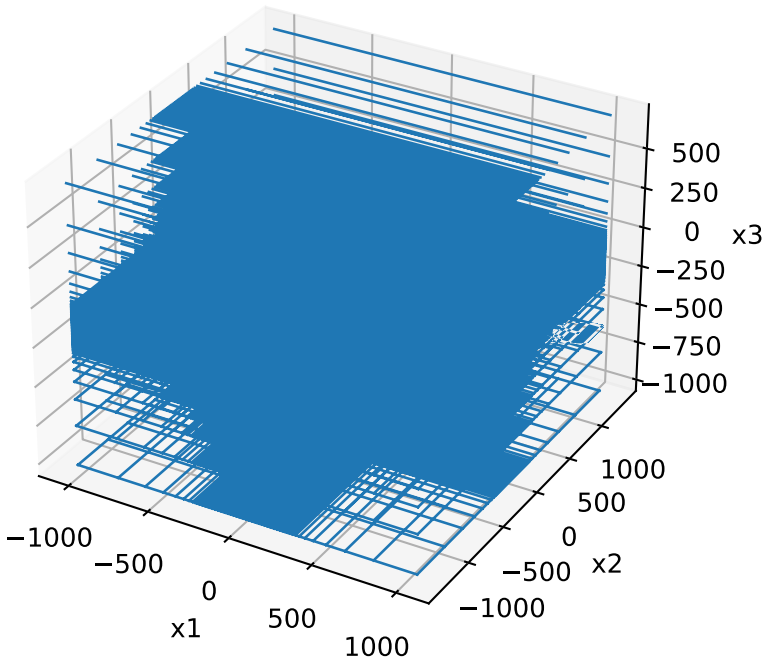

Figure 3.3: 3D tensor mesh generated by SimPEG. The area where we have the block, source and the receivers has been defined densely where the outside of the core domain extended with a padding of 8.

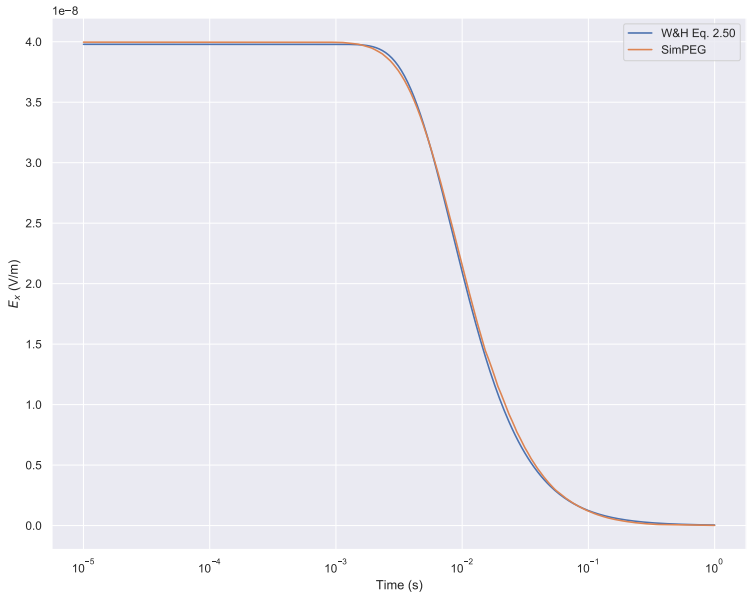

Figure 3.4: Comparison of SimPEG and Ward & Hohmann (1988) Equation 2.50. Both responses calculated for a wholespace with $\sigma = 1$ S/m, and distance between T_{x} and R_{x} is 200 meters.

Figure 3.5 shows the electrical resistivities of the common rock types. As we can see in the table, some earth materials are highly conductive such as massive sulfides and graphite, where some of them are highly resistive such as igneous and metamorphic rocks. This thesis defined a highly conductive unit such as a cover with 100 S/m conductivity or a highly resistive unit such as conductivity of 0.01 S/m. Moreover, in the next section, we investigated the parameter sensitivities, and again, we defined highly conductive/resistive units and/or highly chargeable units. Some of those models might not be geologically realistic. However, in our investigations, we wanted to maximize the signal and apply the method in some extreme cases. Applications of any other geological models would be straightforward.

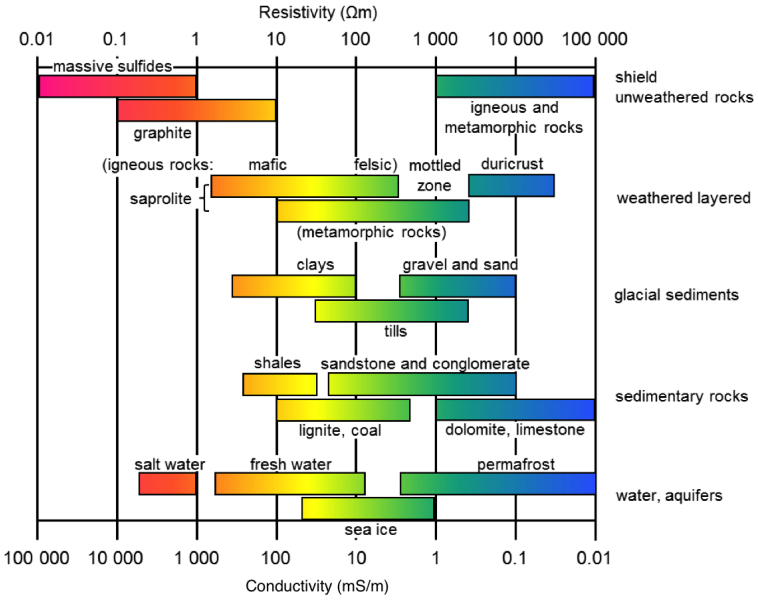

Figure 3.5: Electrical conductivity (and its inverse resistivity) table of the earth materials (From https://em.geosci.xyz/).

3.3 Investigating The Parameters

We will now explore how each parameter behaves and affect the measurements. Each parameter has a different role on the characterization of the IP relaxation. As a physical property of medium, Seigel (1959) defined chargeability η which is the increase in polarization charges in the medium due to an applied current. However, Siegel did not mention anything about the other parameters such as τ and c which define the essence of charging and discharging. This section will investigate each parameter of the IP relaxation and show the simulation results of different parameter values to understand the behavior of IP relaxation controlled by a complex conductivity model.

3.3.1 Parameter σ

Conductivity σ is a physical property of the material and it quantifies how well the electric current flows into the material under an applied electric current. In Equation 2.24, Ohm's law describes the relationship between the current density and the electric field. The electrical conductivity (and its inverse electrical resistivity) depends on the mineralogy of

the rock. Moreover, the electrical current is mostly carried through pore water, thus the ion content of the pore water is also important (Glover, 2015).

We have defined 3 different conductivity models for the block; 5 S/m, 10 S/m and 50 S/m. We kept the background conductivity as $\sigma = 1$ S/m for all 3 simulations. Also, the block is the only chargeable unit with $\eta = 0.3$ V/V. $\tau_{IP} = 0.5$ s, c = 0.25. DC results recorded at t = 0 and DC results do not take τ_{IP} and c into account. However, since the block is chargeable and σ has changed in each simulation, each simulation has generated a different DC response.

Table 3.1: Parameters of the simulated models.

	Air	Background	Model 1	Model 2	Model 3
σ (S/m)	10^{-8}	1	5	10	15
η (V/V)	0	0	0.3	0.3	0.3
τ_{IP} (s)	0	0	0.5	0.5	0.5
c	0.25	0.25	0.25	0.25	0.25

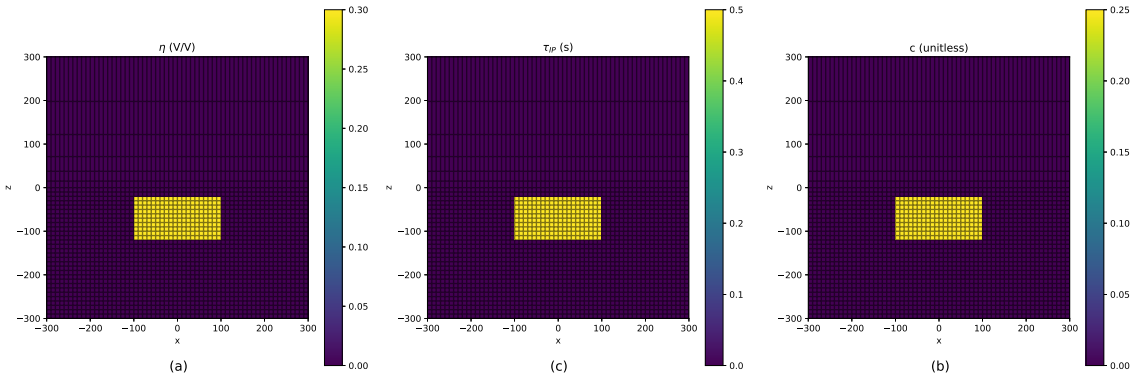

Figure 3.6: Side views of the model. (a) Side view of η model. (b) Side view of τ_{IP} model. (c) Side view of c model.

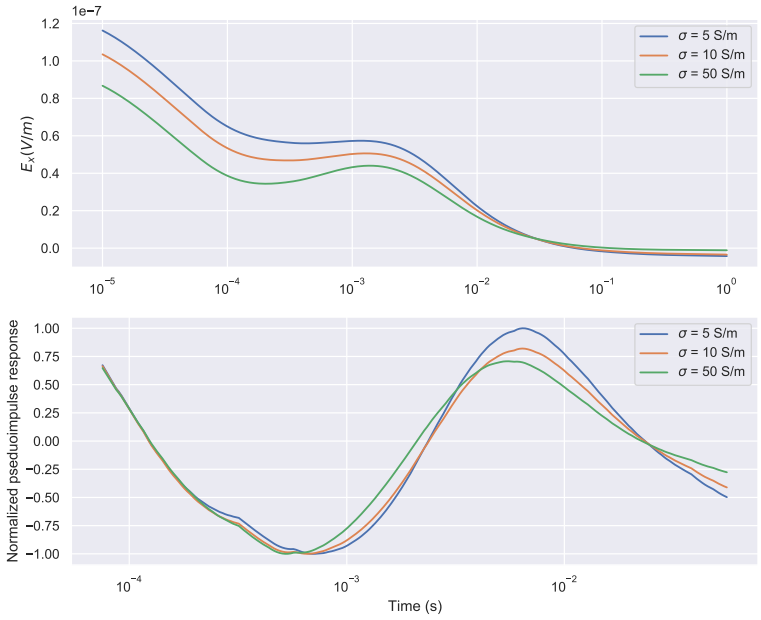

Figure 3.7: E_x curves and the normalized pseudoimpulse responses of 3 different conductivity values where T_x at -250 meters and the R_x at -90 meters.

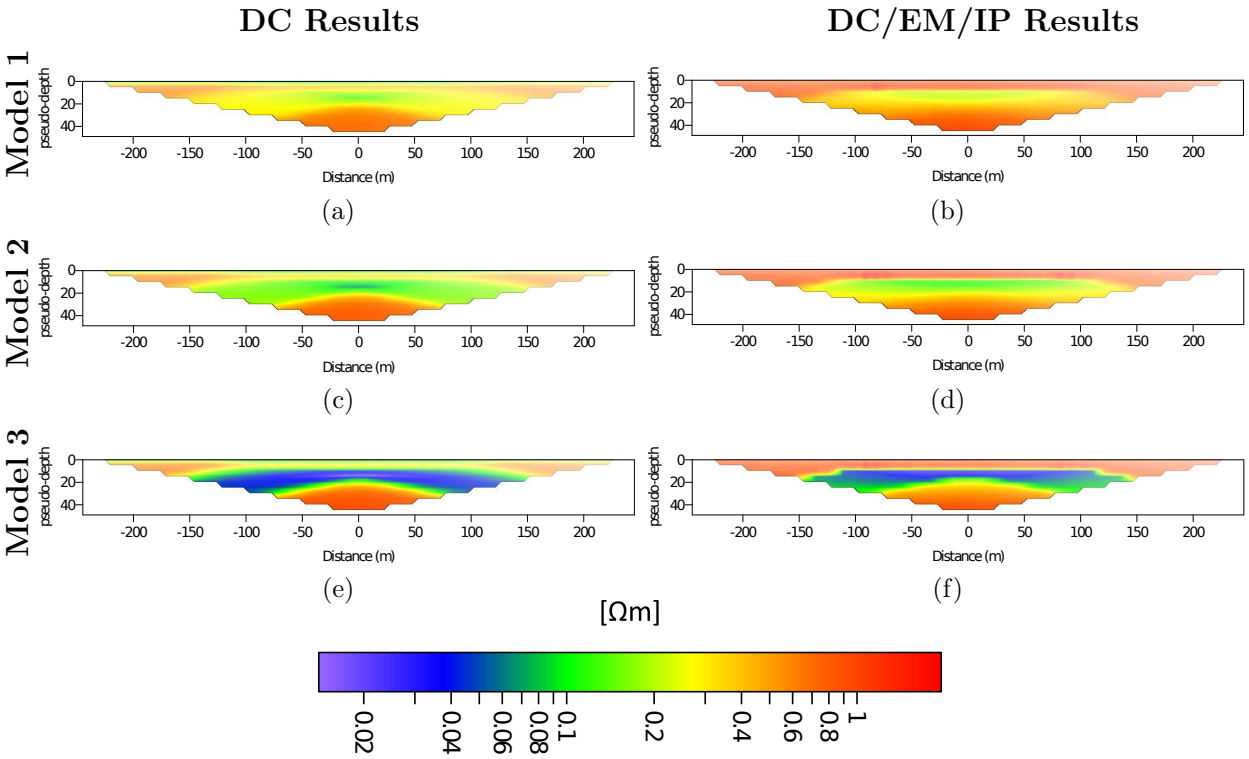

Figure 3.8: Comparison of DC/EM/IP and DC pseudosections of 3 different σ models. I fixed $\eta = 0.3$ V/V, $\tau_{IP} = 0.5$ s and c = 0.25 for all 3 models.

The DC/EM/IP results clearly show that the anomaly of the block becomes more visible when σ increases. The same behavior can be seen in DC sections, since block η is constant and σ has increased from 5 S/m to 50 S/m. The main difference between both techniques is the information content. DC/EM/IP method contains more information than traditional DC/IP method.

Beside those pseudosections, we would like to discuss the results in Figure 3.7. The figure shows E_x curves and Normalized Pseudoimpulse Responses of 3 different conductivity values where the source at -250 meters which is the first source position of the simulation, and the receiver at -90 meters. Since the block's lateral limits are from -100 meters to 100 meters, the recorded field at -90 meters is highly affected by the chargeable block. At lower conductivity, the peak arrival times are not much affected by the presence of chargeability, even if the shape of the pseudoimpulse response has been affected. However, at high conductivity where $\sigma =$ 50 S/m, a shift can be seen on pseudoimpulse response. This result shows that the arrival time is sensitive to the conductivity of the material. Moreover, since the peak arrival time of the pseudoimpulse response is not highly distorted by IP, this method may provide a potential remedy for improving DC and IP results.

3.3.2 Parameter η

We will now investigate the parameter η. Previously mentioned, η is first defined by Seigel (1959) as a physical property related to conductivity. When a current is applied, chargeable materials in subsurface are built-up of ionic charges which is IP. This phenomenon generates electric dipole moments within the rock and under the effect of an electric field, and it helps us to describe the rock formation and strength of the IP inside the chargeable geological unit. We have defined 3 different models to examine how each of those materials impacts the observations. We have used a buried, conductive chargeable block for each simulation. First, we started with a small chargeability, $\eta = 0.1$ V/V, then we increased η to 0.5 V/V and finally to 0.7 V/V which is a highly chargeable.

Table 3.2: Parameters of the simulated models.

	Air	Background	Model 4	Model 5	Model 6
σ (S/m)	10^{-8}	1	10	10	10
η (V/V)	0	0	0.1	0.5	0.7
τ_{IP} (s)	0	0	0.5	0.5	0.5
c	0	0	0.25	0.25	0.25

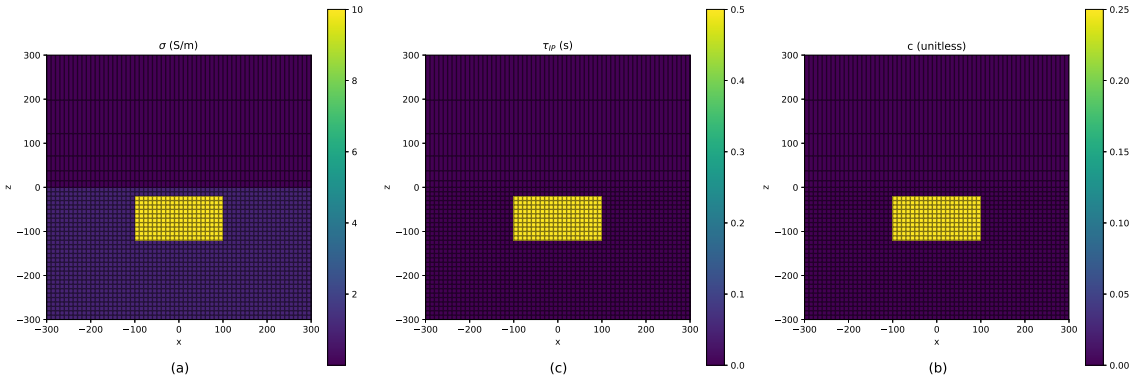

Figure 3.9: Side views of the model. (a) Side view of σ model. (b) Side view of τ_{IP} model. (c) Side view of c model.

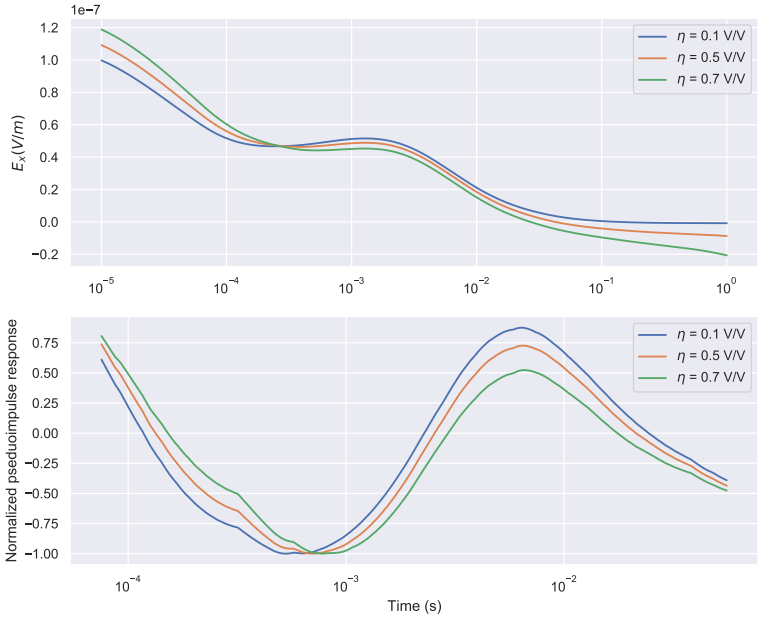

Figure 3.10: E_x curves the normalized pseudoimpulse responses of 3 different η values where T_x at -250 meters and the R_x at -90 meters.

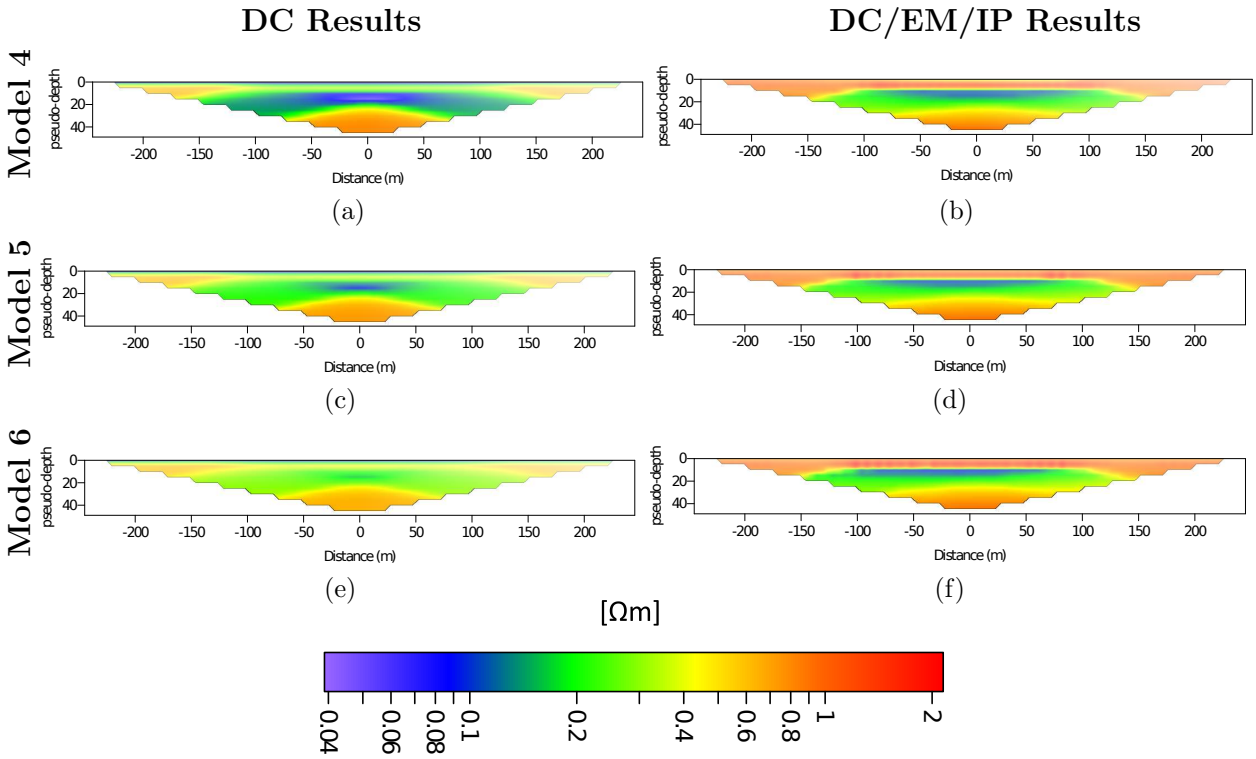

Figure 3.11: Comparison of DC/EM/IP and DC pseudosections of 3 different η models. The block $\sigma = 10$ S/m, $\tau_{IP} = 0.5$ s and c = 0.25 for all 3 models.

First of all, note that as we can see in Figure 3.10, the peak arrival times shifts with chargeability. For different chargeability values, the shape of the normalized pseudoimpulse response changes and we see a shift in the arrival time. The DC/EM/IP method uses the peak arrival time to calculate apparent resistivity ρ_{app} for each source and receiver pair. Since the peak arrival times affected chargeability, we can also see this response in the pseudosections. The DC/EM/IP results can be seen in Figure 3.11(b), Figure 3.11(d) and Figure 3.11(f), with the same color scale. Figure 3.11(f) shows the result when the units are highly chargeable (η = 0.7 V/V) and Figure 3.11(b) shows when the chargeability is 0.1V/V. When η becomes larger, we see a distortion on the plotted image. Moreover, in Figure 3.11(b), the data looks more clear than Figure 3.11(f), where the anomaly got blurred. This may caused by the coupling between the EM and IP, since the normalized pseudoimpulse response is highly sensitive to conductivity and chargeability.

Secondly, DC calculations are directly related with the chargeability. Recall that conductivity at zero frequency is $\sigma_0 = \sigma_\infty(1 - \eta)$. In this case, the larger chargeability will increase the apparent resistivity. As we can see in Figure 3.11(a), Figure 3.11(c) and Figure 3.11(e) the apparent resistivity of the area related to the anomaly has increased by increasing chargeability.

3.3.3 Parameter τ_{IP}

We will now study the effect of the parameter τ_{IP}. τ_{IP} is the time constant of the decay and it defines IP relaxation. To see its effect, We made the background and the block chargeable because the IP signal's strength is related to the target's geometry and size. The block and the background have the same η, τ_{IP} and c. The only difference between them is their conductivities to amplify the parameter's effect and understand how the responses will change. In order to do this, we kept η and c for the background and the block, and we changed τ for both of them in each simulation. We used six different τ_{IP} which are 0.005 s, 0.05 s, 0.5 s, 5 s, 50 s and 500 s. We will only show the results of 0.005 s, 5 s and 500 s, since these three examples will give the general idea.

Table 3.3: Parameters of the simulated models.

	Air	Background	Model 7	Model 8	Model 9
σ (S/m)	10^{-8}	1	10	10	10
η (V/V)	0	0.3	0.3	0.3	0.3
τ_{IP} (s) (block and BG)	0	0.005	0.005	5	500
c	0	0.25	0.25	0.25	0.25

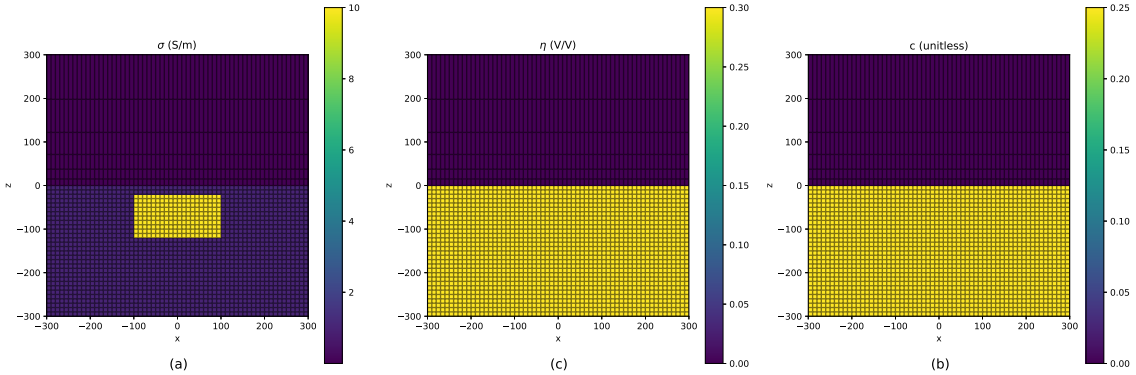

Figure 3.12: Side views of the model. (a) Side view of σ model. (b) Side view of η model. (c) Side view of c model.

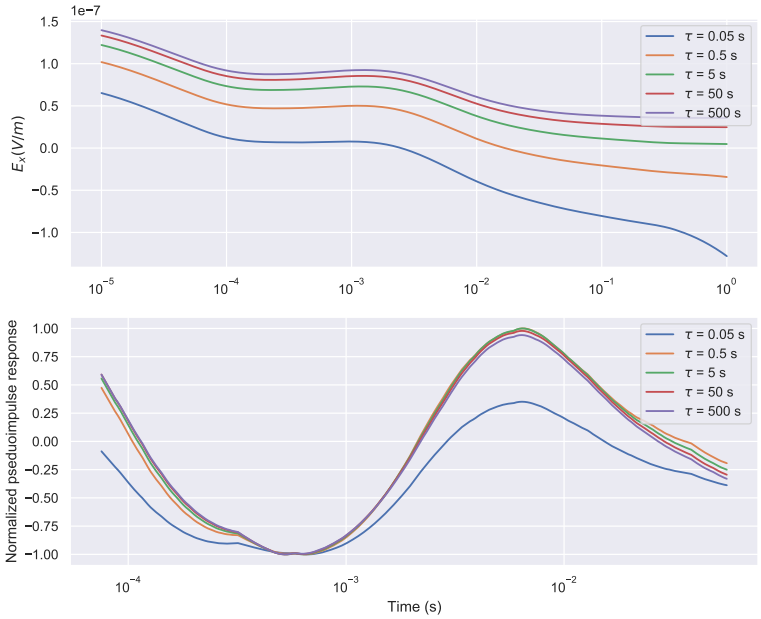

Figure 3.13: E_x curves and the normalized pseudoimpulse responses of different τ_{IP} values where T_x at -250 meters and the R_x at -90 meters.

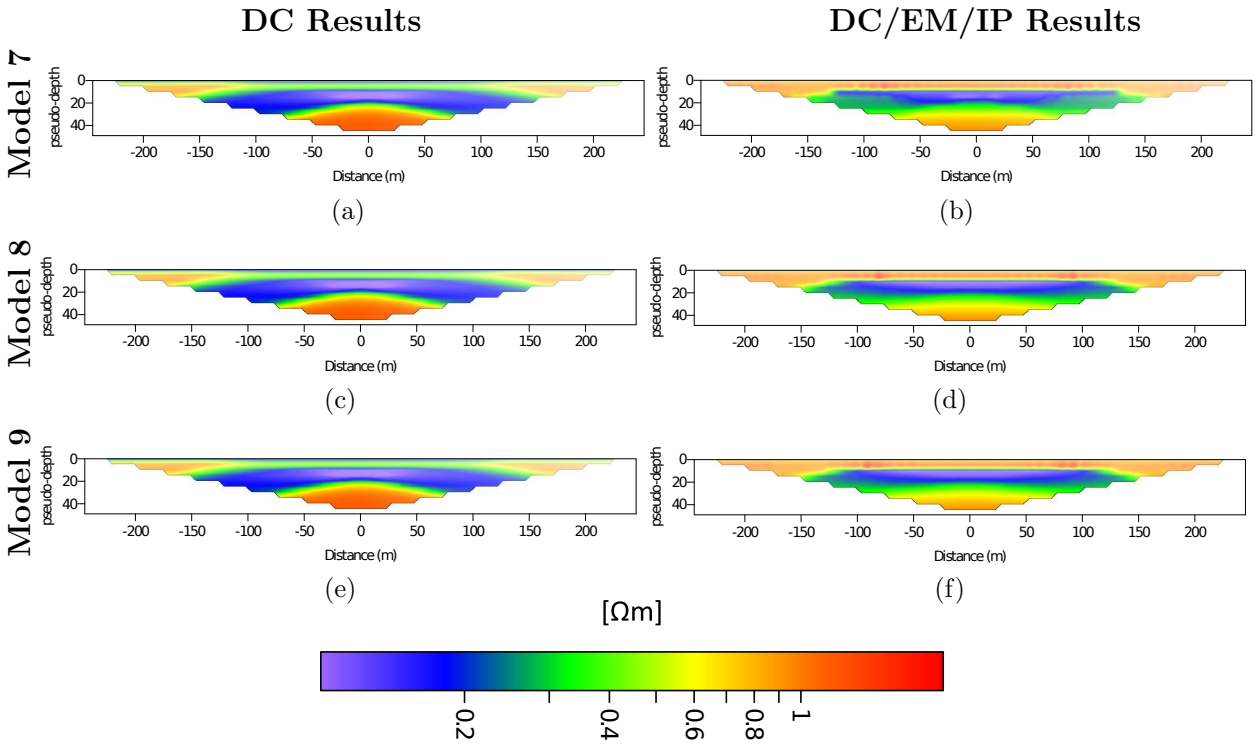

Figure 3.14: Comparison of DC/EM/IP and DC pseudosections of 3 different τ_{IP} models. The block $\sigma = 10$ S/m, $\eta = 0.3$ V/V and c = 0.25 for all 3 models.

Time constant τ_{IP} is probably the most interesting parameter. The relationship between the peak arrival time τ_{EM} and the parameter τ_{IP} directly affects the ρ_{app}. Figure 3.14(f) and Figure 3.14(b) are DC/EM/IP sections of two extreme τ_{IP} values; 500 s and 0.005 respectively. For an extremely small τ_{IP}, EM and IP signals get blended and the apparent resistivity is affected by this effect in the presence of IP. This causes a blurry image in pseudosection. However, in Figure 3.14(f) and Figure 3.14(d), where τ_{IP} is larger than 0.005 s, this effect cannot be seen (or the effect is hard to see). Moreover, where τ_{IP} is 50 s, 5 s, 0.5 and 0.05 still EM arrival is not affected by the presence of IP. Therefore, inverting only EM will probably succeed. On the other hand, for small τ_{IP} values which are where IP and EM signal blend, an EM-only inversion will not be enough. In this case, the coupling between the EM and IP needed to be taken into account of the inversion of grounded source time domain DC/EM/IP data inversion.

Another interesting observation is the DC pseudosection in Figure 3.14(a). Similarly, DC/EM/IP sections provide more information than DC but we also would like to compare the result with Figure 3.19(a) where the block is the only chargeable unit. Both images show similar shapes and a wide anomaly area which makes sense since DC calculations are not affected by τ_{IP} and c. However, since in Figure 3.14(a) the background is also chargeable, the ρ_{app} values are higher, especially for the background due to the natural relationship between DC and IP. In DC, in presence of chargeable material, η reduces the conductivity or in other word, increases the resistivity.

3.3.4 Parameter c

We will now study the parameter c which is Cole-Cole exponent. The parameter c is dimensionless and it governs how broad the relaxation will be. We have used a conductive chargeable block buried in a resistive background and we have simulated 4 different c values; 0.2, 0.5, 0.8 and 1. We fixed the conductivity of the block to 10 S/m and the background conductivity to 1 S/m. Also, in order to increase the effect, We made the background also chargeable. The block and the background chargeability is 0.3 V/V and τ_{IP} is 0.5 s.

Table 3.4: Parameters of the simulated models.

	Air	Background	Model 10	Model 11	Model 12	Model 13
σ (S/m)	10^{-8}	1	10	10	10	10
η (V/V)	0	0.3	0.3	0.3	0.3	0.3
τ_{IP} (s)	0	0.5	0.5	0.5	0.5	0.5
c (block and BG)	0	0.2	0.2	0.5	0.8	1

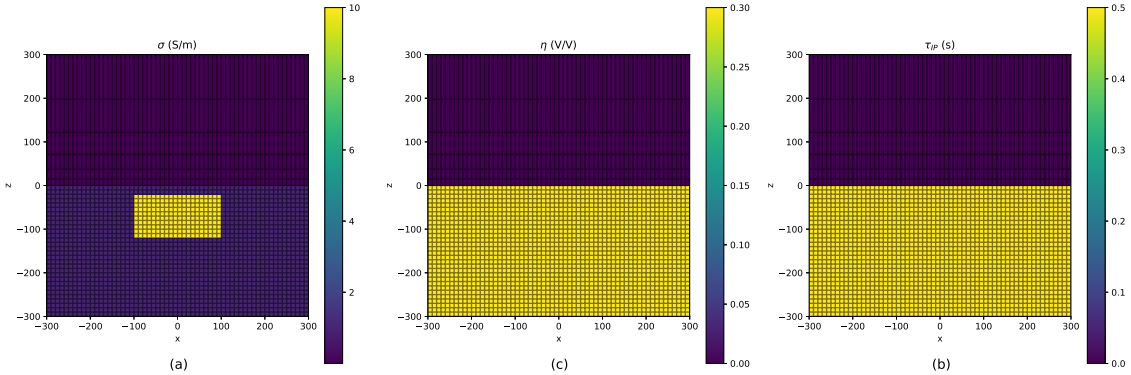

Figure 3.15: Side views of the model. (a) Side view of σ model. (b) Side view of η model. (c) Side view of τ_{IP} model.

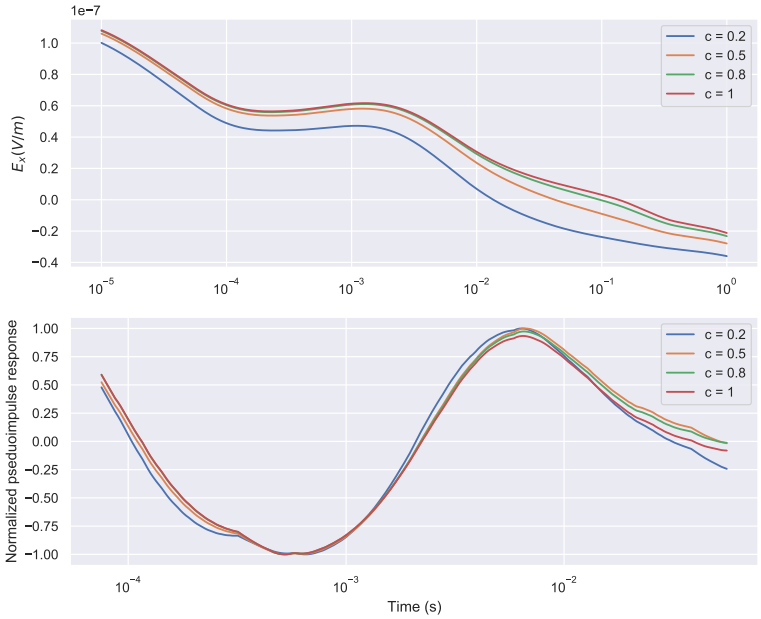

Figure 3.16: E_x curves and Normalized Pseudoimpulse Responses of 4 different c values where T_x at -250 meters and the R_x at -90 meters.

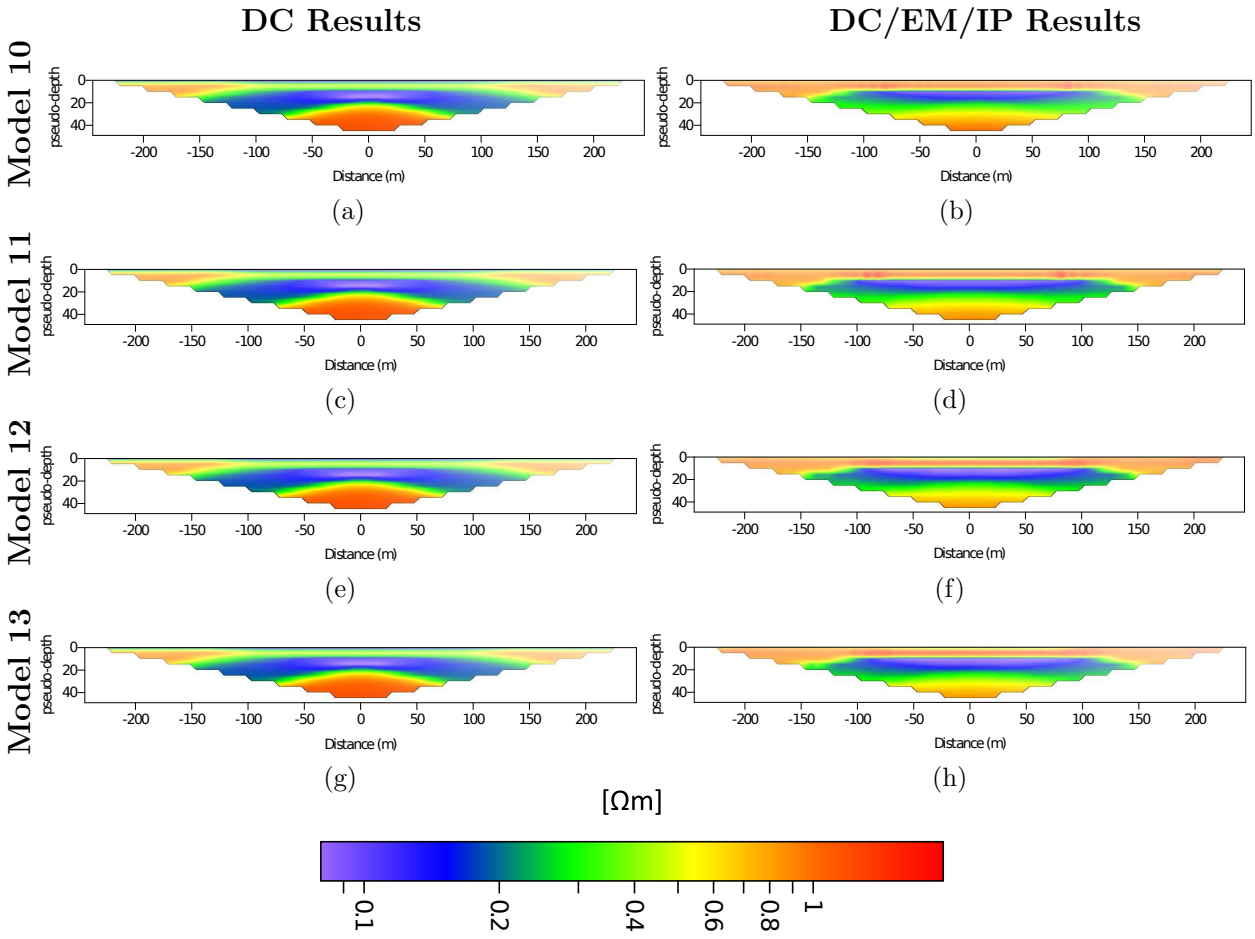

Figure 3.17: Comparison of DC/EM/IP and DC pseudosections of 4 different c models. The block $\sigma = 10$ S/m, $\eta = 0.3$ V/V and $\tau_{IP} = 0.5$ s for all 4 models.

Similar to frequency-domain approach, the relaxation time gets larger when parameter c is smaller. As we can see in Figure 3.16, smaller c generates a relatively broader relaxation. However, it does not cause dramatic changes, especially after the larger values than 0.2. Still, DC/EM/IP response contains more information than DC response. Finally, when c = 1, this is called the Debye model, and both SE and CC models become equal.

3.4 Conductive Chargeable Block in Subsurface

For this model, the air has a conductivity of 10^{-8} S/m which is highly resistive. The background conductivity is 1 S/m, and the conductivity of the block is 10 S/m. The block

is more conductive than the background and the air, where air is the most resistive. While air and the background are not chargeable, the block is chargeable and its chargeability is $\eta = 0.3$ V/V.

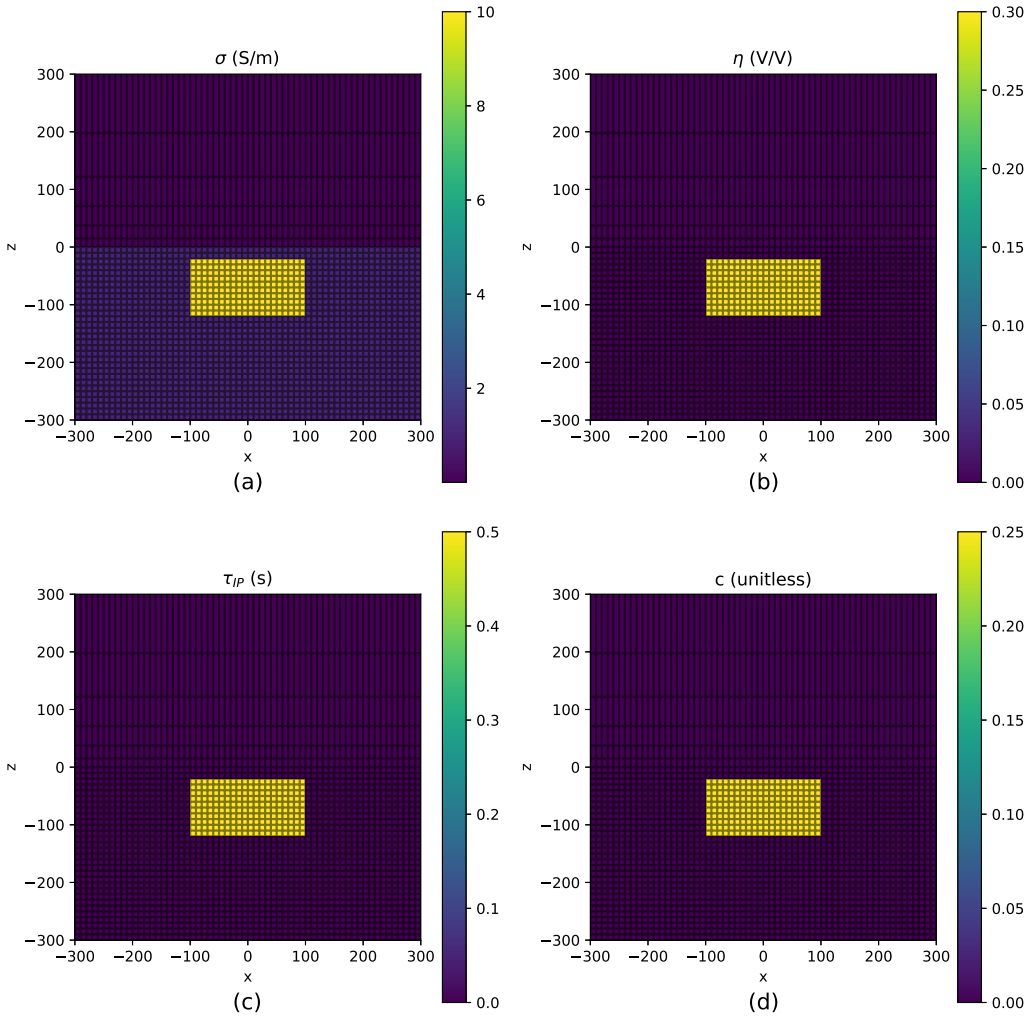

Figure 3.18: Side views and the plan map of the model. (a) Side view of σ model of the conductive block. (b) Side view of η model. (c) Side view of τ_{IP} model. (d) Side view of c model.

3.4.1 Simulation Results

We will now show the simulation results of the buried chargeable block. log_{10} time derivative of the data gives normalized pseudoimpulse response that is explained in Section 3.1.2.

For each source and receiver pair, normalized pseudoimpulse response calculated from the original data contains E_x. The time corresponding to the maximum at normalized pseudoimpulse curve is called τ_{EM} and this parameter can be used in Equation 3.6 to calculate apparent resistivity ρ_{app}.

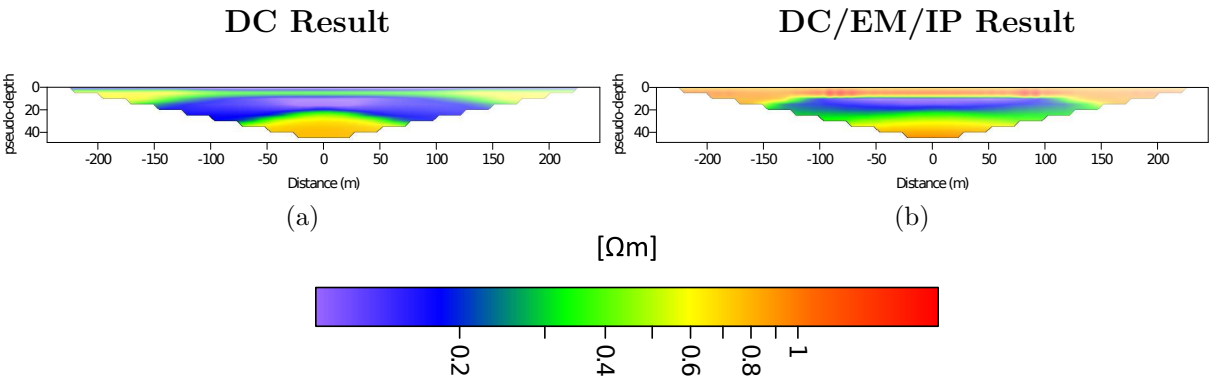

Figure 3.19: Comparison of DC/EM/IP and DC pseudosections of a chargeable conductive block model. The block $\sigma = 10$ S/m, $\eta = 0.3$ V/V, $\tau_{IP} = 0.5$ s, c = 0.25 and the background conductivity is 1 S/m.

These results show that combining EM and IP methods contains more information than a traditional DC measurement in the presence of a conductive chargeable block. In Figure 3.19(b) shows that the DC/EM/IP method clearly shows a higher resistivity contrast between the background and the block in data. Both methods can sense and show the conductive target since both figures show relatively more conductive (or less resistive) areas and the target's symmetry. However, DC/EM/IP method gives a better insight into the target. As we can see in Figure 3.19(b) shows a higher resistivity contrast.

3.5 Resistive Chargeable Block in Subsurface

We will now study a resistive chargeable block in the subsurface to better understand the behavior of the combination of EM and DC/IP on different geoelectrical conditions. Similarly, a 3D block defined in 3D tensor mesh with dimensions of (-100m, 100m) in x, (-100m, 100m) in y direction, and (-20m, -120m) in z directions. The block's conductivity is

1 S/m, and the background conductivity is 10 S/m which is more conductive than the block.

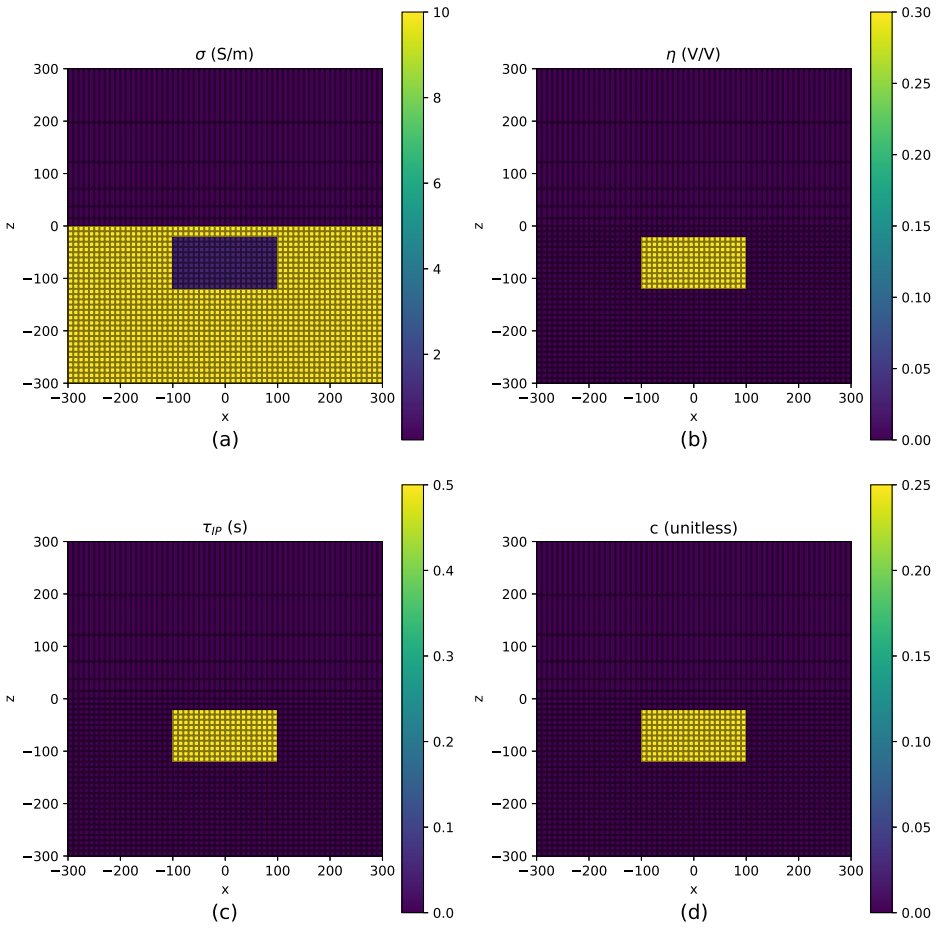

Figure 3.20: Side views and the plan map of the model. (a) Side view of σ model of the resistive block. (b) Side view of η model. (c) Side view of τ_{IP} model. (d) Side view of c model.

3.5.1 Simulation Results

Similar to a conductive chargeable block, We used the same color scale for DC/EM/IP and DC pseuduosections. Recall that we calculated the log_{10} time derivative to convert recorded E_x on each receiver, then used peak arrival time to calculate ρ_{app} with Equation 3.6. For DC ρ_{app} calculation, we used dipole-dipole apparent resistivity formula given in Equation 3.1.

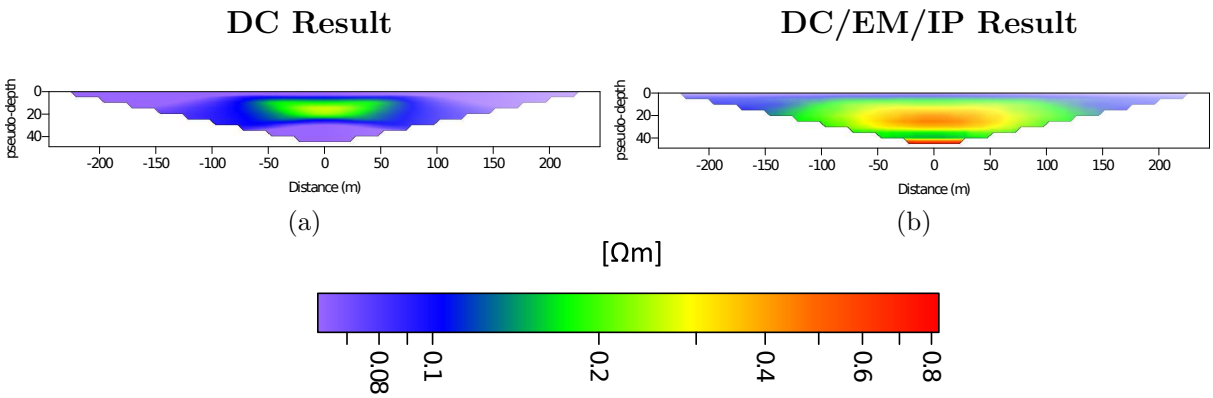

Figure 3.21: Comparison of DC/EM/IP and DC pseudosections of a chargeable resistive block model. The block $\sigma = 1$ S/m, $\eta = 0.3$ V/V, $\tau_{IP} = 0.5$ s, c = 0.25 and the background conductivity is 10 S/m.

The first thing to notice is that both methods generate smooth images when the block is more resistive than the background. In the previous example where the background is more resistive than the target, we could easily see high resistivity contrast in Figure 3.21(b) DC/EM/IP pseudosection. In the presence of a resistive block, the method still gives more information about the target. In both sections, the more resistive area can be seen, but in Figure 3.21(a), the anomaly mostly focused on the center of the target. However, Figure 3.21(b) also shows a transition between -100 meters and 100 meters in x-direction which are the lateral limits of the block. The center of the block shows a higher anomaly with a higher apparent resistivity which is approximately between 0.3 ohm m and 0.4 ohm m. We can see the same apparent resistivity values between -50 meters and 50 meters in x-direction, and it gets smaller as it gets away from the target. Since the background ($\sigma_{\text{background}} = 10$ S/m) is more conductive than the block ($\sigma_{\text{block}} = 1$ S/m), we see those transitions where the receivers away from the center. The DC/EM/IP method uses the bulk arrival times, and the diffusion is faster in a resistive zone (or slower in conductive areas), so both resistive and conductive geological units affect the signal when the receivers are away from the center of the target.

On the other hand, the DC method only shows a small resistive area which is the target's center. Since both sections have plotted on the same color scale, if we look at the ρ_{app} values, we can see that the DC section shows a relatively smaller anomaly between -50 meters and 50 meters on x-direction while DC/EM/IP shows a strong resistivity in the same area. Recall that $\sigma_{DC} = \sigma_{\infty}(1 - \eta)$ so the DC measurements are not affected by τ_{IP} and c, where DC/EM/IP measurements take into account the relaxation parameters.

3.6 Chargeable Block Under A Relatively Conductive Cover

We will now study a chargeable block under a cover that is more conductive than the background. It is challenging to determine a target under a cover in exploration geophysics since the DC signal cannot penetrate relatively resistive or conductive cover where EM signal can penetrate such covers. First, we investigate how the combination of EM and IP will behave in the presence of a cover more conductive than the background above the target; then, we will study the case where the block is beneath a relatively resistive cover. Finally, we will compare the results of the presence and the absence of the cover above the block.

In this exapmle, we kept the cover and the block parameters are the same and made the cover relatively more conductive. We did not explore the responses if we change the parameters of the block and the cover (and maybe even the background) due to several different combinations and the computational time. However, for future research on this kind of scenario, their applications will be straightforward. Moreover, we have shown how the different parameters change the DC/EM/IP responses in previous sections, and they provide an insight into the nature of this complex conductivity modeling.

3.6.1 Parameters of The Model

After exploring and comparing the DC/EM/IP response and DC response for a buried resistive block and a buried conductive block, we will now study where the block has been positioned under a relatively conductive cover. To do this, we defined a highly conductive cover (100 S/m) between the surface and the block. The cover was close to the surface,

positioned at (-30m, -60m) in z, and its thickness is 30 meters. The block is at (-100m, 100m) in x and y directions and (-80m, 180m) in z-direction.

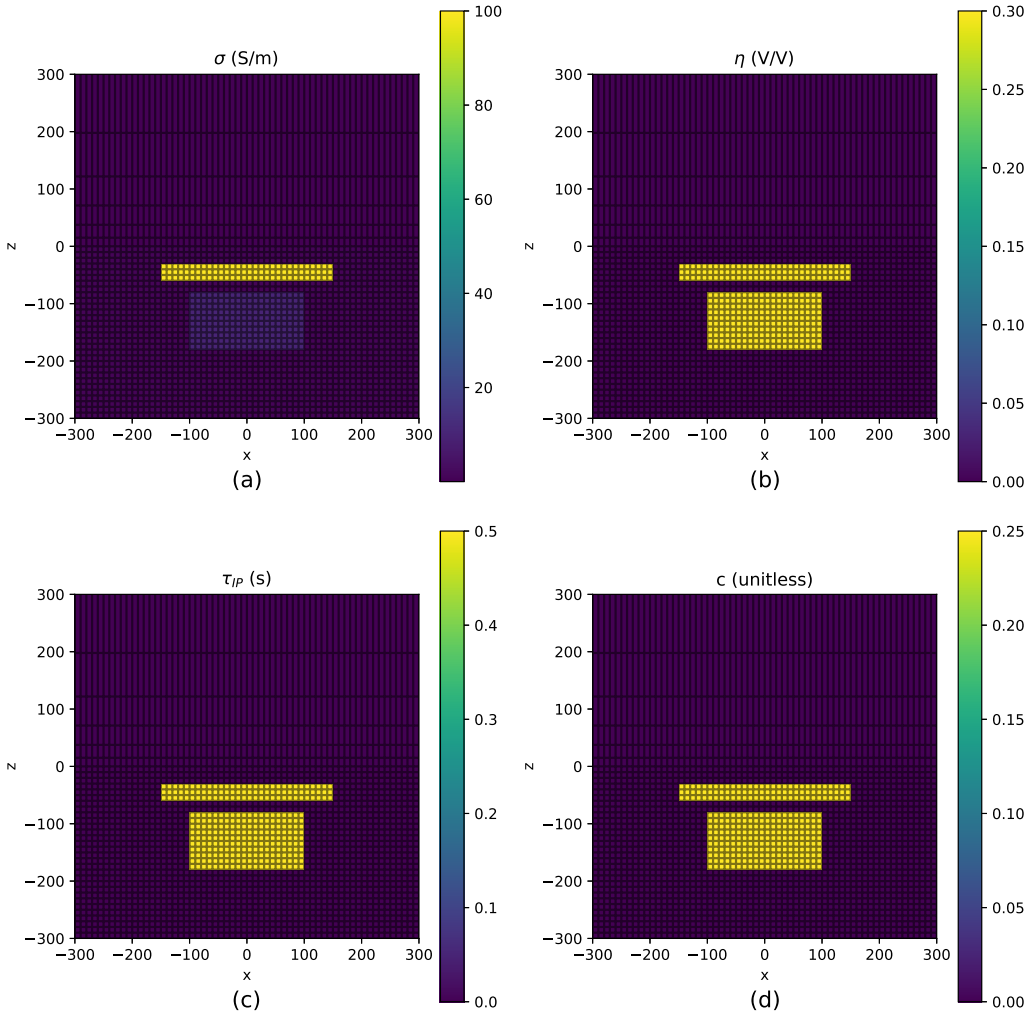

Figure 3.22: Side views and the plan map of the model. (a) Side view of σ mode. (b) Side view of η model. (c) Side view of τ_{IP} model. (d) Side view of c model.

3.6.2 Simulation Results

Interestingly, the DC/EM/IP section in Figure 3.23(b) covers the cover very well. Beneath that relatively conductive cover, a more resistive area can be seen between the value of 0.2 ohm m and 0.3 ohm m. This area is represented with green color in Figure 3.23(b) almost 'spreading' beneath the cover. This anomaly can be caused by the block since the block is

more resistive than the cover. However, if we look at the Figure 3.23(c) and Figure 3.23(d) DC and DC/EM/IP responses of only the cover, respectively, we can clearly see that the section has dominated by the cover. This case, DC/EM/IP did not help and did not show more information about the subsurface than traditional DC.

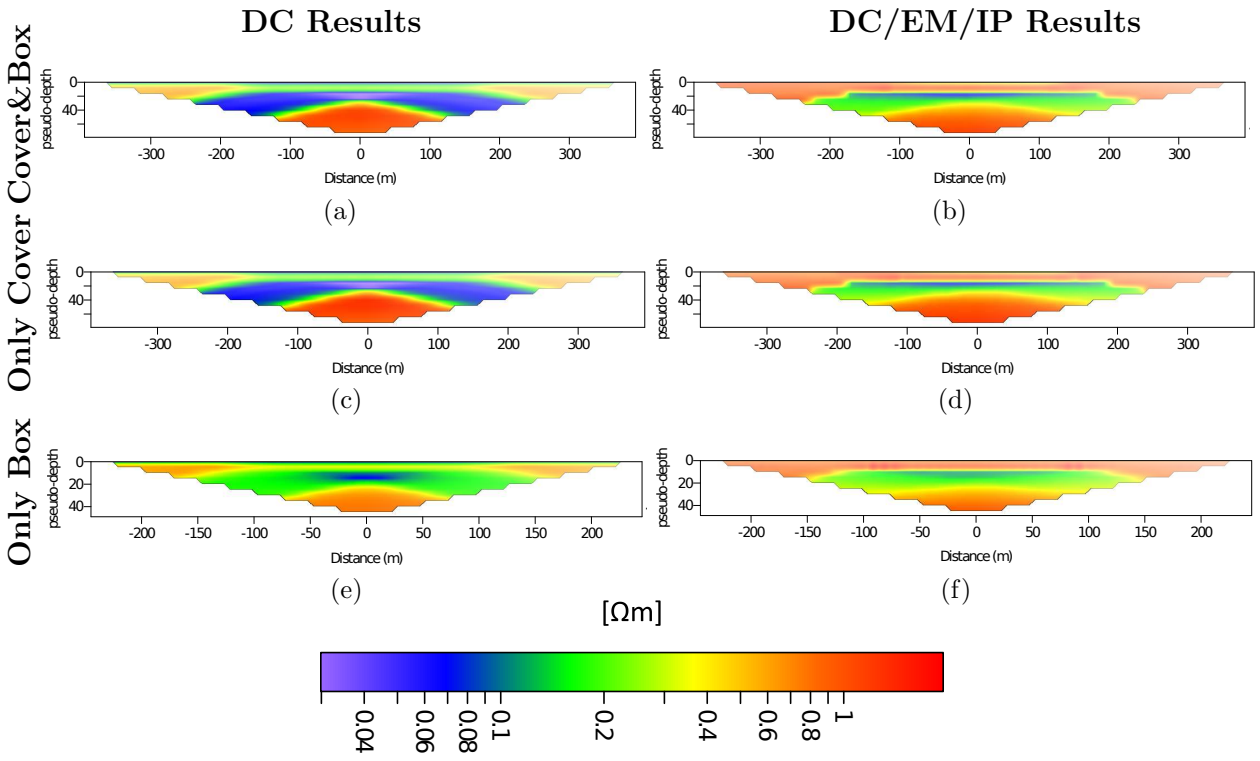

Figure 3.23: Comparison of DC/EM/IP and DC pseudosections in the presence and in the absence of the relatively conductive cover.

3.7 Chargeable Block Under A Relatively Resistive Cover

We will now discuss the simulation results where a 3D chargeable block is buried under a relatively resistive cover. Like a block buried under a relatively conductive cover, the relatively resistive cover is also challenging in subsurface imaging with traditional DC/IP surveys. Since DC signals cannot penetrate such covers, I will investigate if EM signals can penetrate and provide information about beneath the cover.

3.7.1 Parameters of The Model

Here, the cover is relatively more resistive than the background, and the block is the more conductive unit. We fixed the air conductivity to 10^{-8} S/m, where the cover conductivity is 0.01 S/m, and the conductivity of the block is 10 S/m. The background has a conductivity of 1 S/m. As we can see in Figure 3.2(b), we used 81 receivers with 10 meters spacing between -400 meters to 400 meters to increase the aperture of the survey.

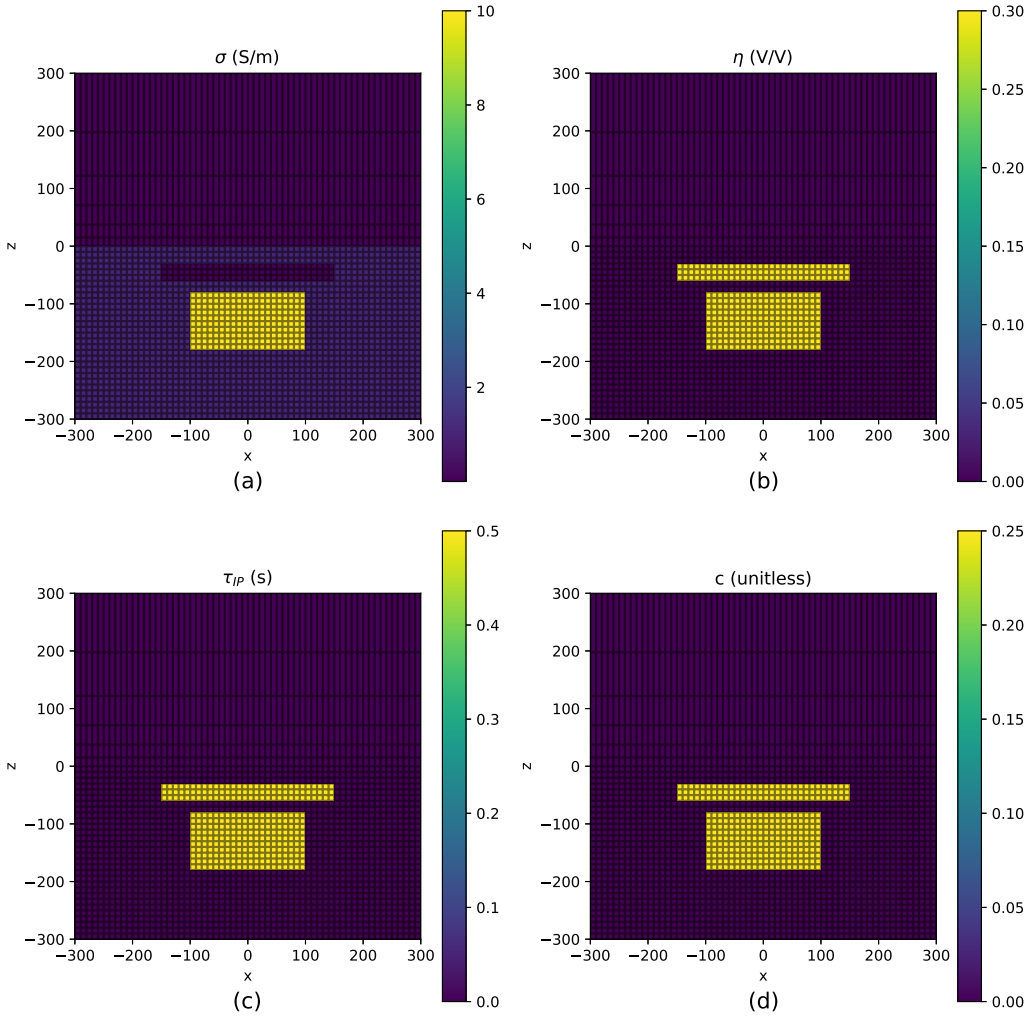

Figure 3.24: Side views and the plan map of the model. (a) Side view of σ mode. (b) Side view of η model. (c) Side view of τ_{IP} model. (d) Side view of c model.

3.7.2 Simulation Results

We compared the pseudosections generated from the DC response and the DC/EM/IP response. Figure 3.25(a) and Figure 3.25(b) show the results when a conductive chargeable block is buried under a resistive cover where Figure 3.25(e) and Figure 3.25(f) show the results without a cover. Interestingly, in the absence of cover, DC/EM/IP sections contains more information than DC section. However, in the presence of a resistive cover, it is difficult to say anything about the block.

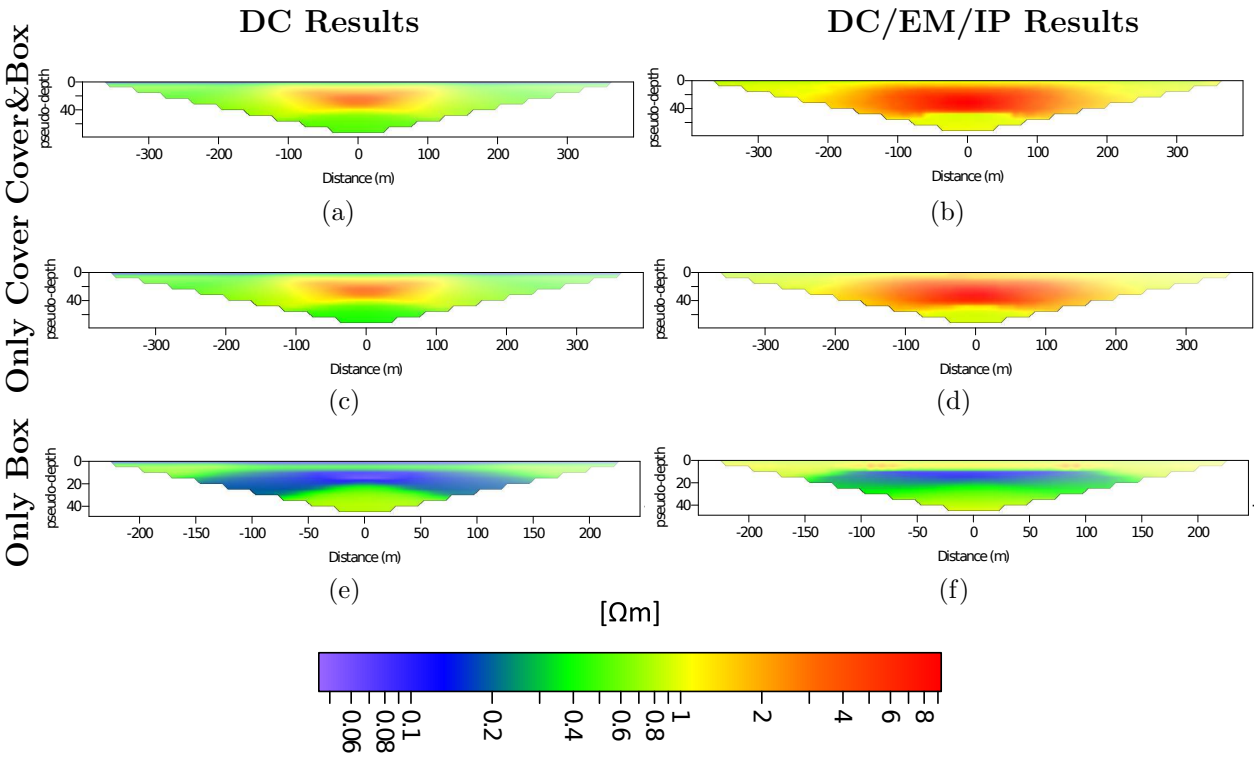

Figure 3.25: Comparison of DC/EM/IP and DC pseudosections in the presence and in the absence of the relatively resistive cover.

Another interesting observation is where we only have the cover. Figure 3.25(c) and Figure 3.25(d) shows the DC result and DC/EM/IP result of only the cover, respectively. The results show that the sections were dominated by the resistive cover in both cases - in the presence of the block and the cover, and when we only have the cover. The highly resistive cover blocks the target, and the current cannot penetrate due to high resistivity.

These results show that in this case, the method underperforms.

3.8 Challenges

In this section, we discuss the challenges that while exploring the possibilities and the responses of the method with different geoelectrical models. I have shown that EM and IP's combination shows promising results for basic geological models such as just a buried block or a block buried under a cover. Moreover, if one performs a full 3D inversion for SE parameters, it is highly possible to produce better subsurface imaging, and this can also create a better understanding of the time characteristic of the IP relaxation and this dynamic EM phenomena IP itself. However, when the geological model becomes more complex than just a block, the developed approach has shown that more research needs to be done due to the complexity of the model.

To illustrate this, we have used a porphyry model. Porphyry deposits are low or medium-grade deposits, and they are essential economic resources. They provide a large amount of silver, gold, copper, and other metals. The model is originally presented by Kang & Oldenburg (2019); we slightly changed it and used it to see how DC/EM/IP method will behave under such geological conditions.

3D porphyry model contains six different geological units, and they are represented with a different color in Figure 3.27. The model looks like ice cream, and it is narrower by depth. The mineralization is between the stock and the cone-like structure is called halo in the model.

Table 3.5: Parameters of air and the six geological units of the porphyry model.

	Air	Background	Overburden	Porphyry	Stock	Mineralization	Halo
σ (S/m)	10^{-8}	10^{-3}	1/900	1/5000	1/4500	1/520	1/500
η (V/V)	0	0	0	0	0	0.1	0.1
τ_{IP} (s)	0	0	0	0	0	5	0.5
c	0	0	0	0	0	0.5	0.5

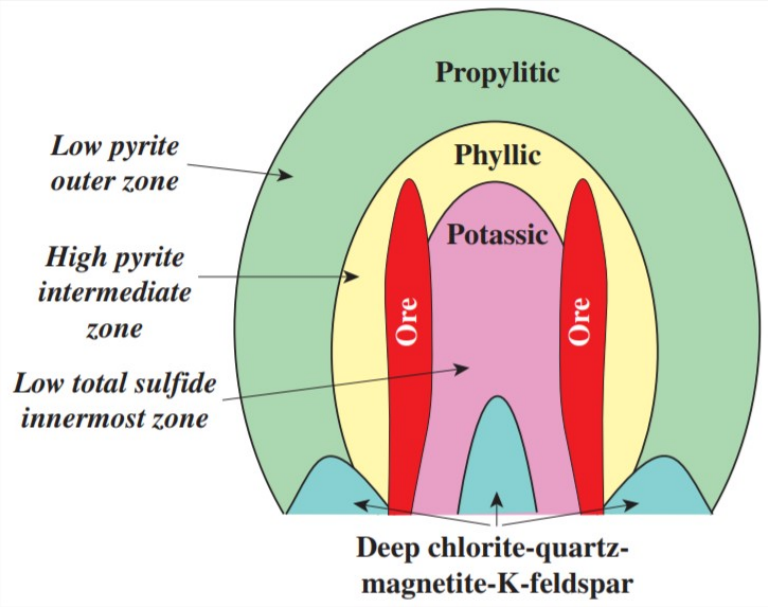

Figure 3.26: Cartoon of a cross section of a porphyry copper deposit (Berger *et al.*, 2008).

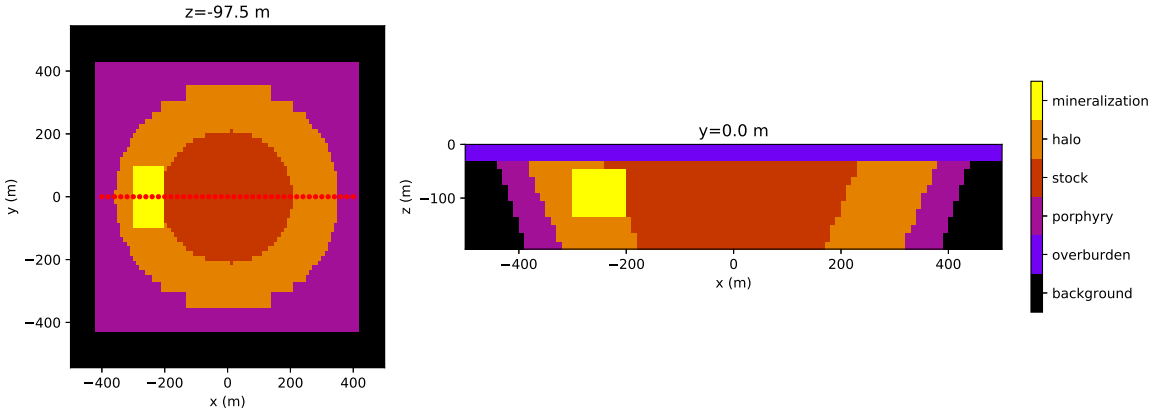

Figure 3.27: Map view and the vertical section of the 3D porphyry model. Plan map on the left shows the top view of the porphyry model at z = -97.5 m. Red dots represent the receivers. Right image shows the six different geological units at y = 0 m.

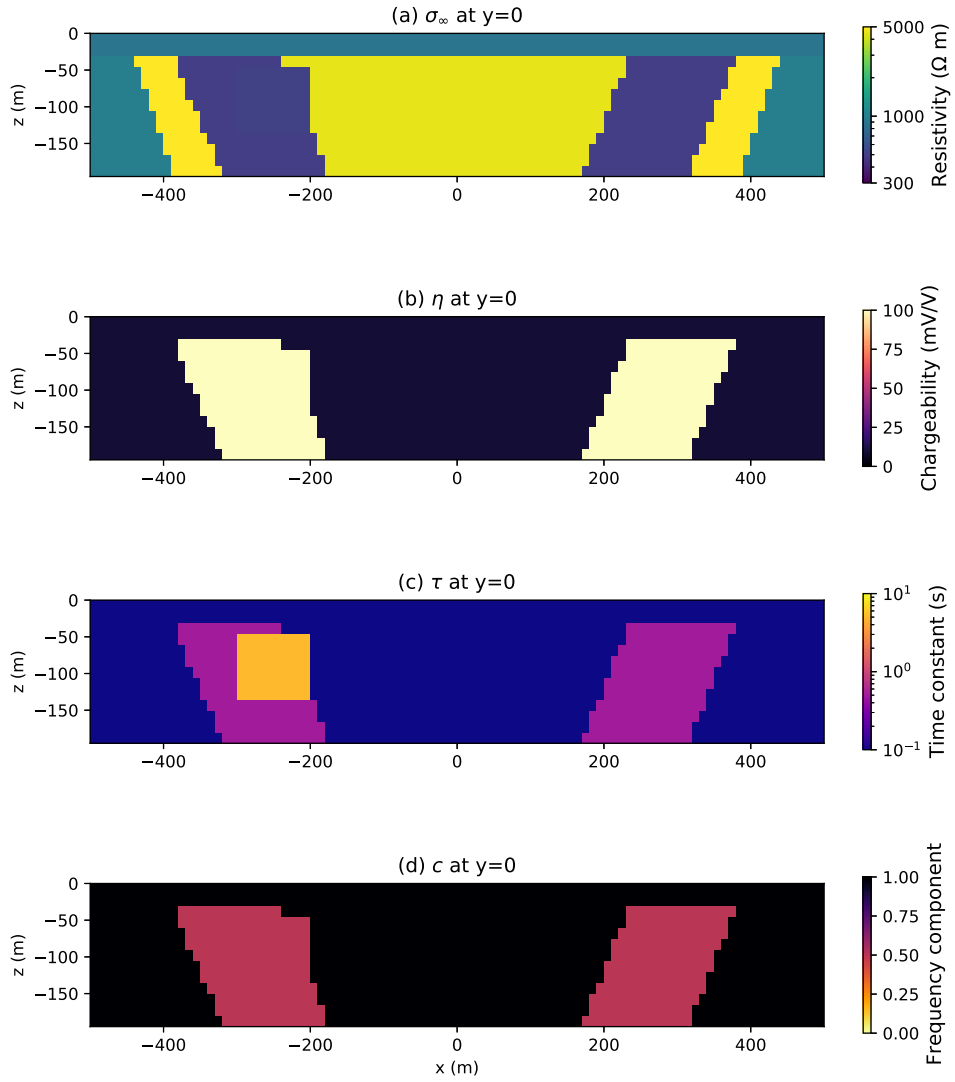

Figure 3.28: Parameters of the six different geological unit in the porphyry model.

We have simulated the porphyry model with a 401 logarithmically spaced time samples from 0 s to 1 s. We used 41 receivers with 20 meters spacing from -400 meters to 400 meters. Since the method is based on the peak arrival time of the E_x, we have taken the derivatives of the each receiver response respect to $\log_{10} t$. Two T_x - R_x responses and their $\log_{10} t$ derivatives can be seen on Figure 3.29 and Figure 3.30; where T_x at -400 meters, R_x at -300 meters and -200 meters, respectively.

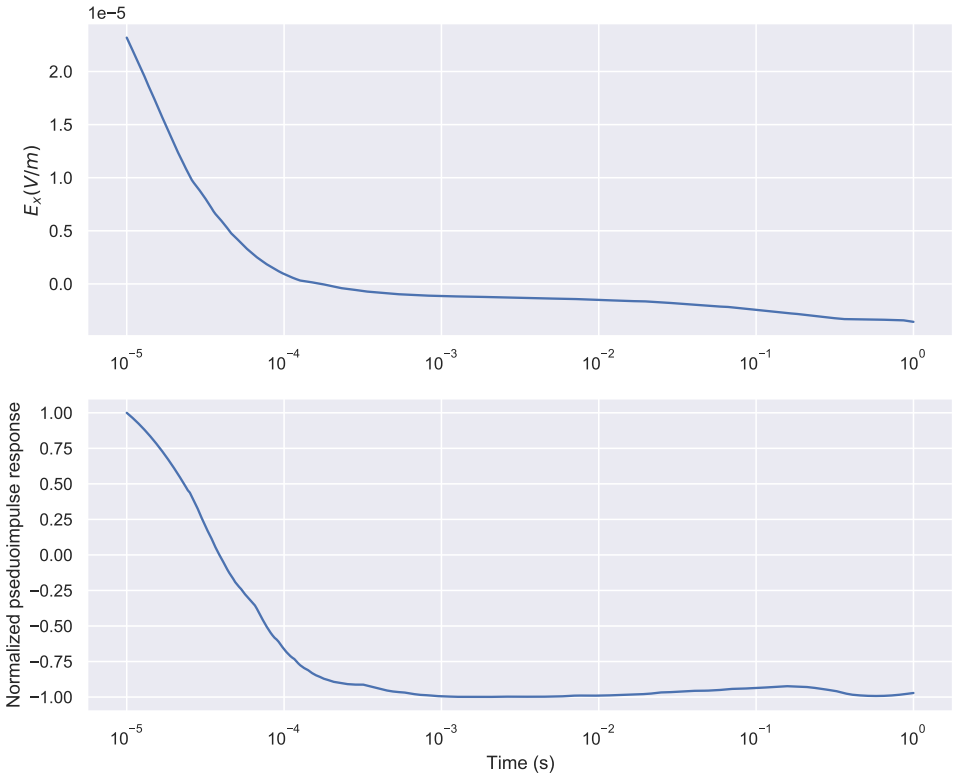

Figure 3.29: E_x and Normalized Pseudoimpulse Response where T_x at -400 meters and R_x at -300 meters.

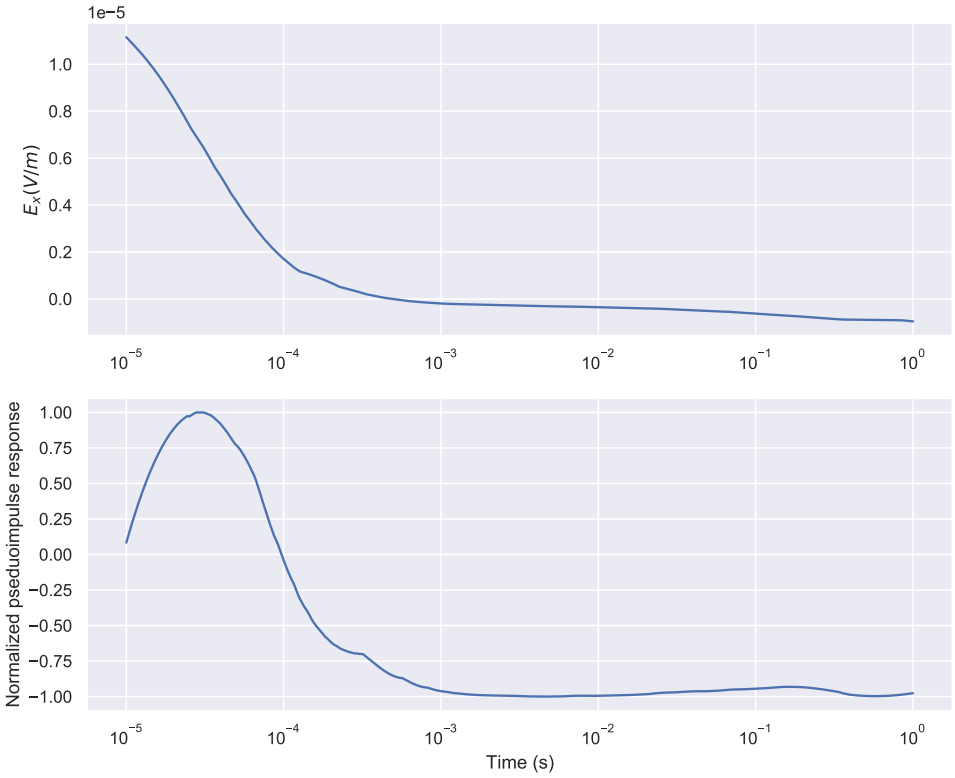

Figure 3.30: E_x and Normalized Pseudoimpulse Response where T_x at -400 meters and R_x at -200 meters.

Interestingly, the field decays fast, and for most of the source-receiver pairs, normalized pseudoimpulse response behaves similarly. The entire model is highly resistive and since the diffusion is fast in resistive zones, everything happens so fast. Since the field decays too early, it is tough to find the peak arrival time. In previous sections, we investigated the parameters, and showed that the peak arrival time is sensitive to conductivity and the presence of the chargeable units. In this model, conductivities are really small, and the only chargeable units are the mineralization and the block. Even if we have a high resistivity contrast, the entire geology is highly resistive and because of this reason, grounded source survey is not performed well. There is still work that needs to be done to effectively use this method on a complex model. Similarly, the method also had problems in the application, in the presence of a relatively resistive or relatively conductive cover. Generally speaking, the cover dominated the entire section and grounded source time domain DC/EM/IP method may not provide more information than traditional DC/IP survey.

CHAPTER 4
PARAMETRIC INVERSION OF GROUNDED SOURCE TIME-DOMAIN DC/EM/IP DATA

4.1 Introduction

Chapter 3 showed and compared the forward modeling results of the grounded source time-domain DC/EM/IP and traditional DC data. In each section, we investigated different geoelectrical and geological models. The results were converted to pseudosections using two fundamental equations; Equation 3.1 for DC pseudosections and Equation 3.5 for DC/EM/IP pseudosections. However, these pseudosections are not the real subsurface image. In geophysics, the data needs to be inverted in order to generate a real subsurface image.

Generally speaking, the inverse problems aim to extract more information about the internal structure of the medium. These estimations are based on the observed data, directly related to unknown parameters and the physical model. In most cases, the inversion's major problem is that the solution is highly sensitive to the noise, which is called ill-posedness. In most cases, an iterative solution is necessary to solve an ill-posed problem.

Especially in the 3D inversion problem, all parameters are unknown for each cell. Moreover, to reconstruct the geology's shape, parameters such as depth need to be considered unknown. This section will only focus on inverting the grounded source time domain DC/EM/IP data to obtain the parameters of a buried conductive chargeable block with a parametric level set method. We used the Levenberg-Marquardt Method to invert grounded source time domain DC/EM/IP data to see if we can obtain the parameters σ, η, τ, and c for a buried conductive chargeable block. However, inverting the data for all the voxels in the model with a full 3D inversion must be the goal for future projects.

4.2 The Levenberg-Marquardt Method

Minimizing a least square problem usually appears in the context of least squares curve fitting. If there is a linear relationship between the model and its parameters, the problem can be solved by a linear matrix equation to obtain the parameters. However, when the relationship is not linear, an iterative solution is required to solve the problem and estimate the parameters.

For m≥n, define a vector function f : $\mathbb{R}^n \mapsto \mathbb{R}^m$. We want to find the minimum of a function f(x) which is a is a sum of squares of nonlinear functions;

$$F(x) = \frac{1}{2}\sum_{i=1}^{m}\big(f_i(x)\big)^2 \tag{4.1}$$

This type of nonlinear least square problem can be solved with iterative methods such as the Gauss-Newton method. The Levenberg–Marquardt Method (LM) is also used to solve non-linear least squares problems. In 1944, the algorithm was published by Kenneth Levenberg (Levenberg, 1944) then in 1963, rediscovered by Donald Marquardt (Marquardt, 1963). As an iterative non-linear least square algorithm, LM finds the local minimum and integrates two numerical minimization algorithms; the Gauss-Newton algorithm and the gradient descent method. The behavior of LM depends on the distance between the parameters and their optimum values. When the parameters are away from their optimum values, LM works like a gradient descent method. When the opposite occurs, it acts like the Gauss-Newton method (Gavin, 2011).

The Levenberg-Marquardt algorithm can be defined as;

$$[J^T W J + \lambda I]h_{lm} = -J^T W f \tag{4.2}$$

to minimizing the $\frac{||Jh+f||_2^2}{2}$ subject to $||h||^2 < \Delta$, where h_{lm} is the model update, f denotes f(x), J is the Jacobian matrix of f(x) with a size of the number of data times number of parameters (MxN), λ is nonnegative scalar called damping parameter, and W is the weighting matrix.

The damping parameter λ defines the behavior of LM; when λ is small, Gauss-Newton update occurs, but when λ is large, it results in a gradient-descent update.

We began the inversion part of this project by coding my own algorithm from scratch. We successfully coded the Levenberg-Marquardt method and tested it with basic curve-fitting. However, in a large-scale operation such as the work that has been done in this thesis, we faced obstacles. The first one is the damping parameter λ. As mentioned before, the value of λ defines the behavior of the algorithm. When it is large, gradient descent update occurs, but the result will be a Gauss-Newton update when it is small. So it is obviously important and needs to be handled carefully. The second problem was boundaries. In an inversion, we usually try to limit physical properties' values because of the physical limits. For example, conductivity cannot be smaller than 0. In order to keep these parameters physically meaningful, we define boundaries. In EM, this boundary can be a log boundary, so the conductivity will always be larger than 0. However, it is challenging when we have multiple parameters, and each parameter needs to be limited to a physical boundary. These two main issues led me to find another way to implement this algorithm to my problem. We found an open-source python package called LMfit (Newville *et al.*, 2014) and inverted grounded source time domain DC/EM/IP data with it.

4.3 Implementation of The Levenberg-Marquardt Algorithm With LMfit

To solve this problem, we inverted grounded source time domain DC/EM/IP data with an open-source python package called LMfit. The main reason for this choice was to use this package to define boundaries for each parameter. This is crucially important because η and c cannot be larger than 1, and any parameters cannot be smaller than 0. Normally, parameters like σ can be bounded with a log barrier to avoid negative values, which is against the nature of physics. Luckily, LMfit can handle boundaries for any parameters of the function by defining the minimum and the maximum limits.

We did not reconstruct the shape of the material, and have only inverted grounded source time domain DC/EM/IP data to obtain the parameters of a conductive chargeable block

buried in a subsurface, since we assumed we already know the shape of the anomaly (which is the block) and the position of the anomaly. To do this, we embedded the block in the subsurface, and updated the block parameters after each iteration.

LMfit is a python wrapper of the 'leastsq' function of python package SciPy (Virtanen *et al.*, 2020), and under the hood, it runs legacy Fortran package MINPACK-1. This algorithm solves the Levenberg-Marquardt method iteratively. In this algorithm, Jacobian is calculated by the forward difference approximation and the approximation of the ith column of the Jacobian matrix can be defined as;

$$\frac{f(x + h_i e_i) - f(x)}{h_i} \tag{4.3}$$

where h_i is the difference parameter and e_i is the ith column of the identity matrix. It uses a user-defined variable called 'epsfcn', used in finding a suitable step length for the forward-difference approximation of the Jacobian and h_i is defined as;

$$h_i = (\text{epsfcn})^{1/2} x_i \tag{4.4}$$

The convergence test of the algorithm is based on the difference between the model and the data. There are three different convergence tests in the algorithm; relative error of the sum of squares (xtol), the relative error of the approximate solution (ftol), and orthogonality between the columns of the Jacobian and the function vector (gtol). The iteration stops when any of the tests are satisfied. For the problem's solution, I have only defined values as stopping criteria for the first two tests, and I fixed xtol and ftol to 10^{-7}.

4.4 Parametric Inversion of Grounded Source Time Domain DC/EM/IP Data

We embedded a conductive chargeable block into a resistive background and fixed the air conductivity to 10^{-8} S/m. Since the Levenberg-Marquardt algorithm is an iterative solver, the main issue is the cost or, in other words, the computation time. To reduce the computation time, we modified the mesh that was originally used for the forward model

simulations. To do this, we defined the cell size as 20 meters in the x-direction, 25 meters in the y-direction, and 20 meters in the z-direction. Furthermore, because of the same reason, we reduced the time steps of the problem. We used 50 logarithmically spaced time steps from 10^{-5} seconds to 1 second.

Table 4.1: Parameters of the true model, initial model and the inversion result.

	True Model	Initial Model	Inversion Result
σ (S/m)	10	25	9.99
η (V/V)	0.3	0.9	0.29
τ_{IP} (s)	0.5	3	0.49
c	0.2	0.8	0.2

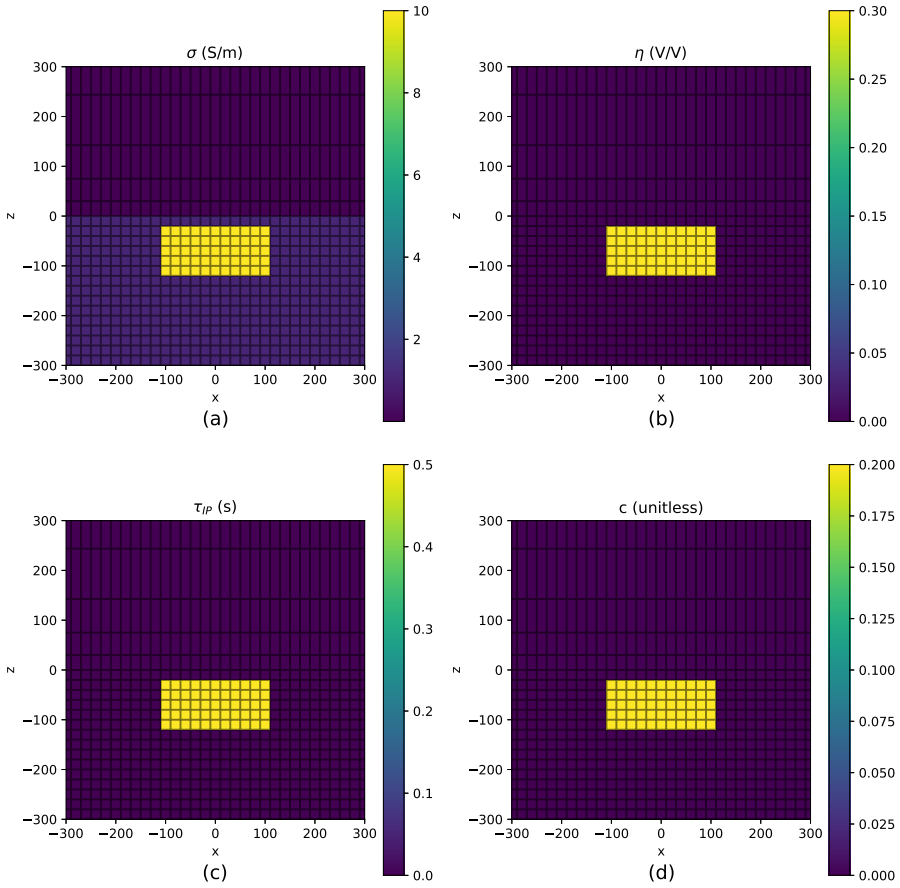

Figure 4.1: Side view of the true model. (a) True σ model. (b) True η model. (c) True τ_{IP} model. (d) True c model.

To generate data, SimPEG EMIP package is used. For the discretization of the 3-D tensor mesh, I define a core region and I use 20 m $\times$ 25 m $\times$ 20 m cell for the core region. Five percent Gaussian noise added to data. I obtain parameters σ, η, τ and c by fitting all of E_x data. Total number of data is 132.651. After 44 iterations, the algorithm can be able to fit the data.

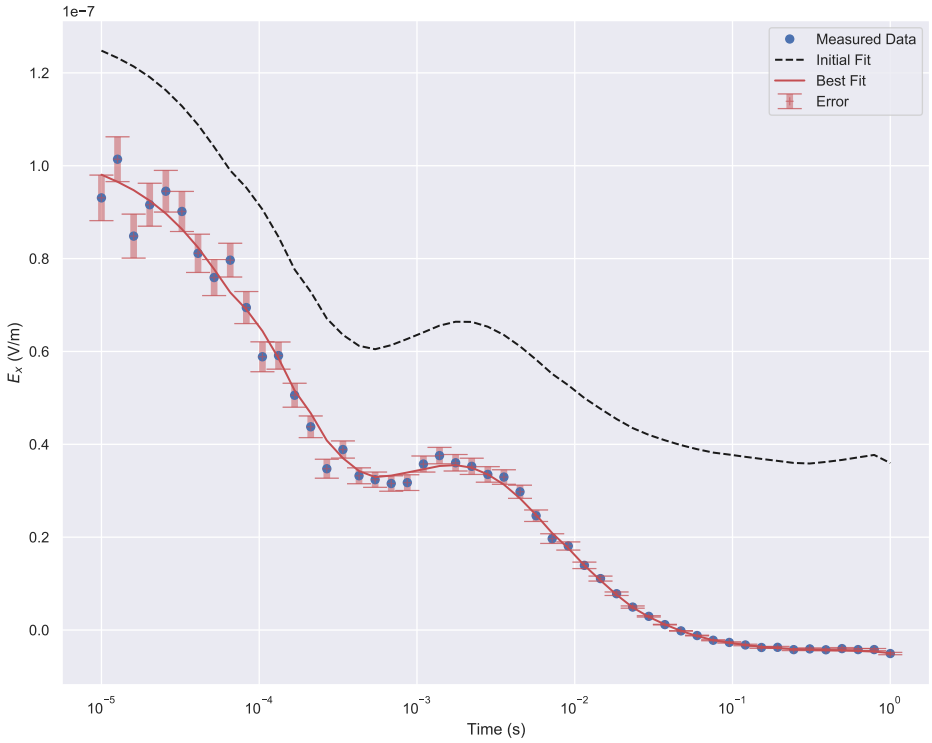

Figure 4.2: Inversion result where T_X at -250 meters and R_x at -90 meters.

We also investigated the importance of the prior knowledge. We defined a new initial model and chose the parameters far away from the true values. The reason is that we wanted to see if we could recover the parameters in this case. The result can be seen in Table 4.2. According to inversion results, the algorithm could not fit the data. This might be a local minimum and this could be the reason of this result. This also show the importance of the prior knowledge when inverting the data. This extra informations can help us to choose a better initial model and this may let us to find more accurate solution.

Table 4.2: Parameters of the true model, initial model and the inversion result.

	True Model	Initial Model	Inversion Result
σ (S/m)	10	250	468.9
η (V/V)	0.3	0.01	0.87
τ_{IP} (s)	0.5	15	744051
c	0.2	0.6	0.88

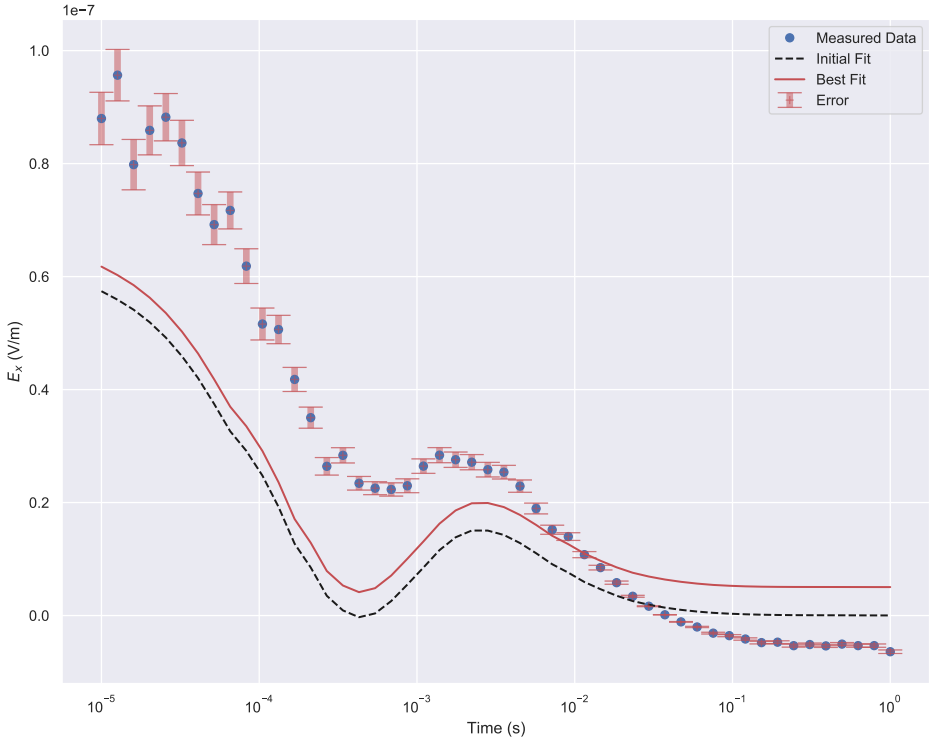

Figure 4.3: Inversion result where T_X at -250 meters and R_x at -90 meters.

4.5 Block Under A Relatively Resistive Cover

We also experimented with other cases such as inverting the block's dept and lateral limits with the parameters or inverting the block and the background parameters. These exercises helped us to understand more about the inversion algorithm and its applications. We will not show the results of these experimental simulations. However, we also questioned if it was possible to invert the block's parameters in the presence of a resistive cover. In Chapter

3, we see that the resistive cover dominated the entire section, and the grounded source time domain DC/EM/IP method may not provide extra information about the subsurface than the traditional DC/IP survey. Here, we show the parametric inversion results when the geological unit is buried under a relatively resistive cover. We used the same parameters and the model that we used in Section 3.7

Figure 4.4 shows the parametric inversion results of the block buried under a relatively resistive cover when the source at -250 meters and the receiver is at -90 meters. We fixed the cover parameters to $\sigma = 0.01$ S/m. $\eta = 0.3$ V/V, $\tau_{IP} = 0.5$ s and c = 0.2 - and ran the algorithm to see if we could recover the block parameters in this situation.

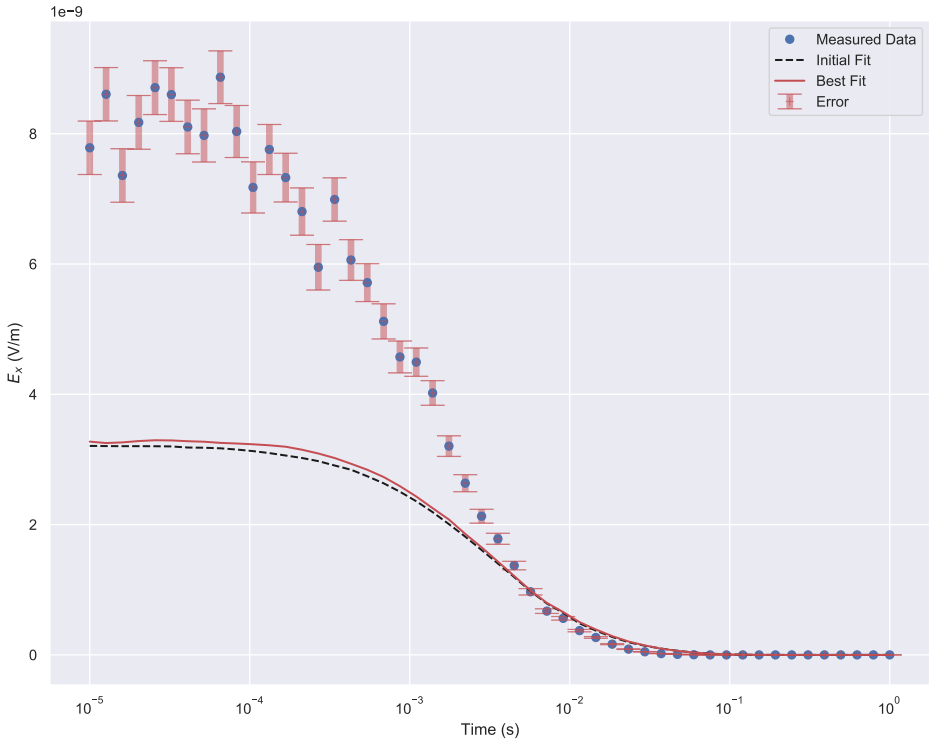

Figure 4.4: Inversion result of in the presence of a relatively resistive cover, where T_X at -250 meters and R_x at -90 meters.

According to these results, the algorithm cannot fit the data when the cover resistivity is 100 times larger than the background resistivity. In the presence of a relatively resistive cover, we could not recover the buried block parameters with only a parametric inversion.

These results also explain why the cover dominates the section and why we cannot see the block anomaly in the forward modeling in Chapter 3. However, if we make the cover 10 times less resistive, we were able to recover the block parameters.

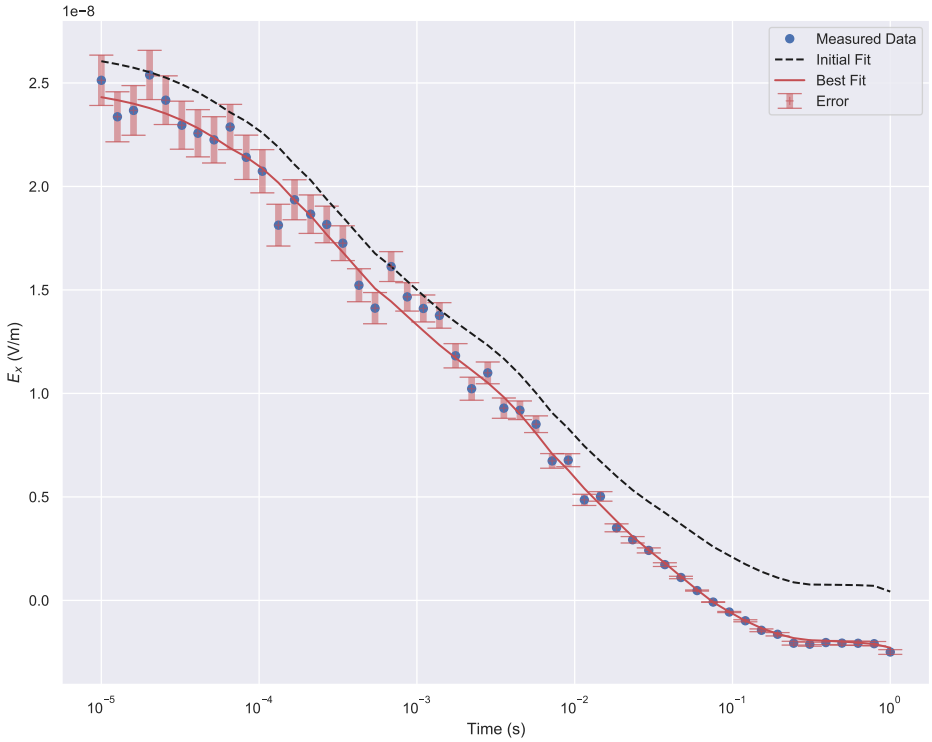

Figure 4.5: Inversion result of in the presence of a relatively resistive cover. The cover conductivity is 0.1 S/m where the background conductivitiy is 1 S/m.

As we can see in Figure 4.5, when the cover is 10 times less resistive than before, we can be able to recover the block parameters.

4.6 Conclusion

We only inverted four parameters for the block. In parametric inversion, we assumed we know the geometry and the position of the block. As we can see in the results, in the absence of a highly resistive or highly conductive cover, grounded source time domain DC/EM/IP data can be inverted to recover the parameters. However, since we only inverted the data to get the block parameters, there is still work that needs to be done to develop

an inversion workflow for grounded source time domain DC/EM/IP data with stretched exponential. Moreover, we see that the parametric inversion algorithm could not recover the block parameters in the presence of a relatively resistive cover. In Chapter 3, we see that the cover dominated the forward model results. This chapter investigated this situation to see if we can invert the grounded source time domain DC/EM/IP data of the buried block under a cover with the Levenberg-Marquard algorithm. The results show that we cannot recover the block parameters in the presence of the cover. 3D inversion techniques need to be developed for the inversion of DC/EM/IP data and this problem might be a good start for the future projects. However, when the cover is 10 times less resistive than before, we were able to recover the block parameters.

With this application, we showed an example to give a simple proof of concept. It is encouraging to recover the parameters for a block from the grounded source time domain DC/EM/IP data. To investigate and learn how to extract better IP information with a stretched exponential approach from grounded source time domain DC/EM/IP data, a lot of work still needs to be done, even if these early results are promising.

CHAPTER 5
CONCLUSIONS

5.1 Conclusions

Throughout this thesis we examined the forward modeling and the parametric inversion of grounded source time domain DC/EM/IP data with using a time domain complex conductivity model is called stretched exponential. In order to understand the natural relationship between the EM and IP, we simulated grounded source time domain DC/EM/IP data with open-source python packages SimPEG and SimPEG-EMIP. We also show grounded source time domain DC/EM/IP data can be inverted. We used the Levenberg-Marquard algorithm to invert the data in order to recover the block parameters.

In Chapter 2, we explaned the theory and the background of IP phenomena, the theory of the coupling between EM and IP, and how this coupling can be effectively used with a modeled grounded source time domain DC/EM/IP data with complex conductivity. Moreover, we show the comparison between the Cole-Cole model and stretched exponential. The results show that they show similar time characteristic.

After we analyzed the each parameters and their effects, we presented computational simulation results of different type of geological and geoelectrical conditions in Chapter 3. At each simulation result, we compared DC/EM/IP results with traditional dipole-dipole DC survey results. DC/EM/IP results contain the EM and IP coupling and calculated with the peak arrival times of the normalized pseudoimpulse response. Normalized pseudoimpulse response is the $\log_{10}$ time derivative of the recorded signal. This response is amplitude independent but highly sensitive to conductivity and chargeability. With this method, we were able to find peak arrival time for each source and receiver pair and this peak arrival time with Equation 3.5 allowed us to calculate ρ_{app}. Moreover, we show that constant "b" can be derived for a halfspace from Equation 4.174 in Ward & Hohmann (1988), as shown in

Appendix. We aim to understand the coupling between EM and IP and show that the signal containing the EM and IP coupling which is generally considered as noise can contain useful information and may help us to understand this multi physical problem that we called IP relaxation. In Chapter 3, we show the simulation results and the generated pseudosections from DC/EM/IP and the DC signal. For a buried conductive or chargeable block, the results of this method contain more information than traditional DC/IP surveys. We also show that this amplitude independent method called normalized pseudoimpulse response is highly sensitive to conductivity. As shown in Section 3.3.1, changing the conductivity causes a shift in arrival time. Since DC/EM/IP approach is directly related to the signal's peak arrival time, these shifts will generate different sections and this provide an insight about the subsurface model. Moreover, as shown in Section 3.3.3, τ_{IP}, the time constant of the decay, is also has a crucial role in the physic of EM and IP coupling. Very small τ_{IP} generates a more blurry image due to blending of EM and IP signals with each other. We also show the challenges on the application in this chapter. It is difficult to find corresponding peak arrival time on the porphyry model due to generally high resistive units because decay occurs fast. The complex geological model, and the low conductivity might be the reason. Another obstacle observed is in the presence of a highly resistive or highly conductive cover. These problems can open new paths for future researches. Maybe other source types such as a loop source can be used or both data can be combined. Finally, we discussed the parametric inversion of the grounded source time domain DC/EM/IP data with stretched exponential approach so future applications and investigations may be built up on this prior knowledge.

In Chapter 4, we show that grounded source time domain DC/EM/IP data with stretched exponential can be inverted. We only applied a parametric inversion technique and we assumed we know the position and the geometry of the box. We only apply a parametric inversion workflow but the results are promising. We were able to recover the block parameters in the absence of a highly resistive cover. On the other hand, we show that in the presence of a relatively resistive cover, parametric inversion grounded source time domain

DC/EM/IP data to recover the buried block parameters did not work. Full 3D inversion of grounded source time domain DC/EM/IP data would be needed in order to understand the IP relaxation modeled with stretched exponential. Furthermore, it is necessary to recover these parameters from a 3D inversion to see the possible advantages of this technique. However, when we made the cover 10 times more conductive (or less resistive), we were be able to recover the parameters of the block which is positioned below the cover. It is possible to extract more information about subsurface and better conductivity and chargeability model. However, the biggest challenge of this inverse problem is the non-uniqueness due to multi-parameter. How to find the best way to handle this problem is an open question for future researches.

5.2 Speculations

Grounded source time domain DC/EM/IP data show a potential to improve traditional DC surveys. EM coupling can provide additional information about the subsurface. In Chapter 3, forward model results show that the DC/EM/IP method provides more information about the subsurface units than traditional DC/IP method in the absence of a cover. Moreover, in Chapter 4, we inverted grounded source time domain DC/EM/IP data with a parametric level set approach. However, we also show the challenges of applying grounded source time domain DC/EM/IP survey. First, when the block is under a relatively resistive cover, the resistive zone dominates the section, and it makes it harder to see beneath the cover. In the presence of a relatively conductive cover, the same behavior can be seen. Using or combining different source types might be helpful. We only used the galvanic source type in the simulations, but using a loop source or maybe even combining the galvanic source data and the loop source data may help solve this problem. Similarly, for the 3D porphyry case, the same idea could be implemented.

We can also speculate that the problem with complex geology or the geological unit buried under a cover might be the sensitivity. Since we use the normalized pseudoimpulse response, which is the log10 time derivative of the E_x for data reduction, we picked each source and

receiver pairs' peak arrival time. It would be worth investigating the entire dataset, and maybe some other parts of the data might be sensitive to geological units that this method has challenged.

It is also important to note that we only inverted grounded source time domain DC/EM/IP data of a block embedded in the subsurface. We assumed we know the block position, depth, and shape. Under these assumptions, we recovered the parameters of the block. These results are promising, but we think the ultimate goal must be a full 3D inversion to understand better. Inverting the data for each voxel with a developed technique will help to understand this phenomenon better. On the other hand, developing an inversion workflow for this non-unique multi-parameter inversion would be the real challenge.

5.3 Future Works

This work investigates the coupling between EM and IP in grounded source time domain DC/EM/IP data with stretched exponential. With SE, we allowed to model the complex conductivity and the IP relaxation in time domain. We investigated the physical behaviour of the each parameter and have modeled different geological cases such as buried conductive chargeable block, buried resistive chargeable block. The results shows that EM coupling in IP can be used and interpreted instead of considering as noise. Chapter 3 shows that forward modeling results show the potential of this method. However, there are still some challenges due to complexity of the geological model. Especially on highly resistive zones, it will be necessary to investigate the complex conductivity parameters and IP relaxation. Throughout this thesis, we have used galvanic source type and it may be worth a try to use different source types to understand more about this phenomena.

Future work to be continued directly from this project relate to inversion of grounded source time domain DC/EM/IP data with complex conductivity. In Chapter 4, we inverted the grounded source grounded source time domain DC/EM/IP data with stretched exponential with Levenberg-Marquardt algorithm. With this method, we only inverted the parameters of a block embedded in halfspace with a parametric level set method. 3D inver-

sion of grounded source time domain DC/EM/IP data can provide a better insight about the method. A developed 3D inversion methodology for this method can provide a better chargeability model and more information about the subsurface can be extracted.

REFERENCES CITED

Abramowitz, M., & Stegun, I.A. 1964. *Handbook of Mathematical Functions with Formulas, Graphs, and Mathematical Tables*. Applied mathematics series. U.S. Government Printing Office.

Aiken, C. L., Hastings, D. A., & Sturgul, J. R. 1973. Physical and Computer Modeling of Induced Polarization. *Geophysical Prospecting*, **21**(4), 763–782.

Beard, L. P., & Tripp, A. C. 1995. Investigating The Resolution of IP Arrays Using Inverse Theory. *Geophysics*, **60**(5), 1326–1341.

Belliveau, P., & Haber, E. 2018. Coupled Simulation of Electromagnetic Induction and Induced Polarization Effects Using Stretched Exponential Relaxation. *Geophysics*, **83**(2), WB109–WB121.

Berger, B. R., Ayuso, R. a., Wynn, J. C., & Seal, R. R. 2008. Preliminary Model of Porphyry Copper deposits. *Open-File Report - U. S. Geological Survey*.

Bertin, J., & Loeb, J. 1976. *Experimental and Theoretical Aspects of Induced Polarization*. 1, no. v. 2. Gebrüder Borntraeger.

Burtman, V., Fu, H., & Zhdanov, M. S. 2014. Spectral Induced Polarization Effect In Unconventional Reservoir Rocks. *Pages 907–911 of: Society of Exploration Geophysicists International Exposition and 84th Annual Meeting SEG 2014*.

Cole, K. S., & Cole, R. H. 1941. Dispersion and Absorption n Dielectrics I. Alternating Current Characteristics. *The Journal of Chemical Physics*, **9**(4), 341–351.

Collet, L.S., Brant, A.A., Bell, W.E., Ruddock, K.A., Seigel, H.O., & Wait, J.R. 1959. Chapter 5 - Laboratory Investigation of Overvoltage. *Pages 50–69 of:* Wait, J. R. (ed), *Overvoltage Research and Geophysical Applications*. International Series of Monographs on Earth Sciences. Pergamon.

Commer, M., & Newman, G. 2004. A Parallel Finite-Difference Approach for 3D Transient Electromagnetic Modeling with Galvanic Sources. *Geophysics*, **69**(5), 1192–1202.

Council, National Research. 1996. *Rock Fractures and Fluid Flow: Contemporary Understanding and Applications*. Washington, DC: The National Academies Press.

Debye, P.J.W. 1929. Polar Molecules. *Journal of the Society of Chemical Industry*, **48**(43), 1036–1037.

Edwards, R. N. 1997. On the Resource Evaluation of Marine Gas Hydrate Deposits Using Sea-Floor Transient Electric Dipole-Dipole Methods. *Geophysics*, **62**(1), 63–74.

Fox, R. C., Hohmann, G. W., Killpack, T.J., & Rijo, L. 1980. Topographic Effects in Resistivity and Induced-Oolarization Surveys. *Geophysics*, **45**(1), 75–93.

Freedman, R., & Vogiatzis, J. P. 1986. Theory of Induced-Polarization Logging in a Borehole. *Geophysics*, **51**(9), 1830–1849.

Gaver, D. P. 1966. Observing Stochastic Processes, and Approximate Transform Inversion. *Operations Research*, **14**(3), 444–459.

Gavin, H. 2011. The Levenberg-Marquardt Method For Nonlinear Least Squares Curve-Fitting Problems. *Department of Civil and Environmental Engineering, Duke University*, **28**, 1–5.

Glover, P. W.J. 2015. Geophysical Properties of the Near Surface Earth: Electrical Properties. *Pages 89–137 of: Treatise on Geophysics: Second Edition*, vol. 11.

Guptasarma, D. 1983. Effect of Surface Polarization on Resistivity Modeling. *Geophysics*, **48**(1), 98–106.

Haber, E., Ascher, U. M., & Oldenburg, D. W. 2004. Inversion of 3D Electromagnetic Data in Frequency and Time Domain Using an Inexact All-At-Once Approach. *Geophysics*, **69**(5), 1216–1228.

Heagy, L. J., Cockett, R., Kang, S., Rosenkjaer, G. K., & Oldenburg, D. W. 2017. A Framework For Simulation And Inversion in Electromagnetics. *Computers & Geosciences*, Oct, 1–19.

Hilfer, R. 2002. H-function Representations For Stretched Exponential Relaxation And non-Debye Susceptibilities In Glassy Systems. *Phys. Rev. E*, **65**(Jun), 061510.

Hohmann, G. W., & Newman, G. A. 1990. Transient Electromagnetic Responses of Surficial, Polarizable Patches. *Geophysics*, **55**(8), 1098–1100.

Kang, S., & Oldenburg, D. W. 2016. On Recovering Distributed IP Information From Inductive Source Time Domain Electromagnetic Data. *Geophysical Journal International*, **207**(1), 174–196.

Kang, S., & Oldenburg, D. W. 2019. Inversions of Time-Domain Spectral Induced Polarization Data Using Stretched Exponential. *Geophysical Journal International*, **219**(3), 1851–1865.

Kohlrausch, R. 1854. Theorie Des Elektrischen Rückstandes in Der Leidener Flasche. *Annalen der Physik*, **167**(1), 56–82.

Kozhevnikov, N. O., & Antonov, E. Y. 2021. On The Equivalence of The Conductivity and Resistivity Equations In The Interpretation of Induced Polarization Data. *Geophysical Prospecting*, **69**(4), 872–877.

Levenberg, K. 1944. A Method For The Solution of Certain Non-Linear Problems In Least Squares. *Quarterly of Applied Mathematics*, **2**(2), 164–168.

Li, Y., & Oldenburg, D. W. 2000. 3-D Inversion of Induced Polarization Data. *Geophysics*, **65**(6), 1931–1945.

Macnae, J. 2015. Comment on: Tarasov, A. Titov, K., 2013, On the use of the Cole–Cole equations in spectral induced polarization, Geophys. J. Int., 195, 352–356. *Geophysical Journal International*, **202**(1), 529–532.

Marchant, D. 2015. *Induced Polarization Effects In Inductive Source Electromagnetic Data*. Ph.D. thesis, University of British Columbia.

Marchant, D., Haber, E., & Oldenburg, D. W. 2014. Three-Dimensional Modeling of IP Effects in Time-Domain Electromagnetic Data. *Geophysics*, **79**(6), E303–E314.

Marquardt, D. W. 1963. An Algorithm for Least-Squares Estimation of Nonlinear Parameters. *Journal of the Society for Industrial and Applied Mathematics*, **11**(2), 431–441.

Marshall, D. J., & Madden, T. R. 1959. Induced Polarization, A Study of Its Causes. *Geophysics*, **24**(4), 790–816.

Newville, M., Ingargiola, A., Stensitzki, T., & Allen, D. B. 2014. LMFIT: Non-Linear Least-Square Minimization and Curve-Fitting for Python. *Zenodo*.

Oehler, D. Z., & Sternberg, B. K. 1982. Induced Polarization For Hydrocarbon Exploration: Geochemical/Geological Interpretation. *Seg Technical Program Expanded Abstracts*, 445–448.

Oldenburg, D. W., & Li, Y. 1994. Inversion of Induced Polarization Data. *Geophysics*, **59**(9), 1327–1341.

Pelton, W. H., Ward, S. H., Hallof, P. G., Sill, W. R., & Nelson, P. H. 1978. Mineral Discrimination And Removal of Inductive Coupling With Multifrequency IP. *Geophysics*, **43**(3), 588–609.

Revil, A., Abdel, A., Gamal Z., Atekwana, E. A., Mao, D., & Florsch, N. 2015. Induced Polarization Eesponse of Porous Media With Metallic Particles - Part 2: Comparison With a Broad Database of Experimental Data. *Geophysics*, **80**(5), D539–D552.

Routh, P. S., & Oldenburg, D. W. 2001. Electromagnetic Coupling In Frequency Domain IP Data: A Method For Removal. *2000 SEG Annual Meeting*, **145**(1), 59–76.

Savitzky, A., & Golay, M. J.E. 1964. Smoothing and Differentiation of Data by Simplified Least Squares Procedures. *Analytical Chemistry*, **36**(8).

Seigel, H., Nabighian, M., Parasnis, D. S., & Vozoff, K. 2007. The Early History of The Induced Polarization Method. *Leading Edge*, **26**(3), 312–321.

Seigel, H. O. 1959. Mathematical Formulation And Type Curves For Induced Polarization. *Geophysics*, **24**(3), 547–565.

Smith, R. 2016. Induced Polarization Effects In Airborne Alectromagnetic Data: Estimating Chargeability From Shape Reversals. *Pages 2211–2217 of: SEG Technical Program Expanded Abstracts.*

Stehfest, H. 1970a. Algorithm 368: Numerical Inversion of Laplace Transforms [D5]. *Commun. ACM*, **13**(1), 47–49.

Stehfest, H. 1970b. Remark on Algorithm 368: Numerical Inversion of Laplace Transforms. *Commun. ACM*, **13**(10), 624.

Sumner, J.S. 1976. *Principles of Induced Polarization for Geophysical Exploration.* Developments In Economic Geology, vol. 5. Elsevier Scientific.

Swidinsky, A., Hölz, S., & Jegen, M. 2015. Rapid Resistivity Imaging for Marine Controlled-Source Electromagnetic Surveys With Two Transmitter Polarizations: An Application To The North Alex Mud Volcano, West Nile Delta. *Geophysics*, **80**(2), E97–E110.

Tarasov, A., & Titov, K. 2013. On The Use of The Cole-Cole Equations In Spectral Induced: Polarization. *Geophysical Journal International*, **195**(1), 352–356.

Towle, J. N., Anderson, R. G., Pelton, W. H., Olhoeft, G. R., & LaBrecque, D. 1985. Direct Detection of Hydrocarbon Contaminants Using The Induced-Polarization Method. *Pages 145–147 of: 1985 SEG Annual Meeting, SEG 1985.*

Van Voorhis, G. D., Nelson, P. H., & Drake, T. L. 1973. Complex Resistivity Spectra of Porphyry Copper Mineralization. *Geophysics*, **38**(1), 49–60.

Virtanen, P.and Gommers, R., Oliphant, T. E., Haberland, M., Reddy, T., Cournapeau, D., Burovski, E., Peterson, P., Weckesser, W., Bright, J., van der Walt, S. J., Brett, M., Wilson, J., Millman, K. J., Mayorov, N., Nelson, A. R. J., Jones, E.and Kern, R., Larson, E., Carey, C J, Polat, I., Feng, Y., Moore, E. W., VanderPlas, J., Laxalde, D., Perktold, J., Cimrman, R., Henriksen, I., Quintero, E. A., Harris, C. R., Archibald, A. M., Ribeiro, A. H., Pedregosa, F., van Mulbregt, P., & SciPy 1.0 Contributors. 2020. SciPy 1.0: Fundamental Algorithms for Scientific Computing in Python. *Nature Methods*, **17**, 261–272.

Wait, J.R. 1959. Chapter 4- The Variable-Frequency Method. *Pages 29 – 49 of:* Wait, James R. (ed), *Overvoltage Research and Geophysical Applications*. International Series of Monographs on Earth Sciences. Pergamon.

Ward, S. H. 1967. 2. Part A. Electromagnetic Theory for Geophysical Applications. *Pages 13–196 of: Mining Geophysics, Volume II, Theory*.

Ward, S. H. 1990. Resistivity and Induced Polarization Methods. *Pages 147–190 of: Geotechnical and Environmental Geophysics*.

Ward, S.H., & Hohmann, G. W. 1988. 4. Electromagnetic Theory for Geophysical Applications. *Pages 130–311 of: Electromagnetic Methods in Applied Geophysics*.

Weller, A., Nordsiek, S., & Bauerochse, A. 2006. Spectral Induced Polarisation - A Geophysical Method for Archaeological Prospection in Peatlands. *Journal of Wetland Archaeology*, **6**(1), 105–125.

Zhdanov, M. 2008. Generalized Effective-Medium Theory of Induced Polarization. *Geophysics*, **73**(5), F197–F211.

Zonge, K., Wynn, J., & Urquhart, S. 2005. Resistivity, Induced Polarization, and Complex Resistivity. *Pages 265–300 of: Near-Surface Geophysics*.

Zonge, K. L., & Wynn, J. C. 1975. Recent Advances And Applications In Complex Resistivity Measurements. *Geophysics*, **40**(5), 851–864.

APPENDIX

ARRIVAL TIMES IN A HALFSPACE

Consider an electric dipole carrying a current I and having a length ds. For homogeneous earth, the response due to a step function current in time domain can be found in equation 4.174 in Ward & Hohmann (1988) as;

$$E_{inline}^{step} = Ids\Big[-p(\rho) + \frac{\partial^2 q(\rho)}{\partial x^2}\Big] \tag{A.1}$$

with

$$q(\rho) = \frac{1}{2\pi\sigma\rho}u(t) \tag{A.2}$$

and

$$p(\rho) = \frac{1}{2\pi\sigma\rho^3}\Big[erf(\theta\rho) - \frac{2}{\sqrt{\pi}}\theta\rho e^{-\theta^2\rho^2}\Big] \tag{A.3}$$

where $\rho^2 = x^2 + y^2 + z^2$, $\theta = \sqrt{\mu\sigma/4t}$, σ is conductivity and μ is magnetic permeability of homogeneous earth. Inline impulse response can be obtained by taking the time derivative of the step response;

$$E_{inline}^{impulse} = \frac{\partial E_{inline}^{step}}{\partial t} = Ids\frac{2\mu\theta e^{-\theta^2\rho^2}}{\sqrt[3]{\pi}t^2} \tag{A.4}$$

Pseudoimpulse response $E_{inline}^{pseudoimpulse}$ can be defined as the derivative of the step response with respect to logarithmic time (Edwards, 1997);

$$E_{inline}^{pseudoimpulse} = \frac{\partial E_{inline}^{step}}{\partial log_{10}t} = 2.302 \times t\frac{\partial E_{inline}^{step}}{\partial t} \tag{A.5}$$

When the time derivative of Equation A.4 is equal to zero, the peak arrival time τ of the inline impulse response can be found. This differentiation can be defined as;

$$\frac{\partial E_{inline}^{impulse}}{\partial t} = Ids\frac{\mu\theta e^{-\theta^2\rho^2}(\mu\sigma\rho^2 - 10t)}{2\sqrt[3]{\pi}t^4} \tag{A.6}$$

Equation A.6 is goes to zero when $\mu\sigma\rho^2 - 10\tau = 0$, or when $\tau = \frac{\mu\sigma\rho^2}{10}$. Similarly, pseudoimpulse response, the peak arrival time occurs when time derivative of Equation A.5 goes to zero.

$$\frac{\partial E_{inline}^{pseudoimpulse}}{\partial t} = 2.302 \times Ids\frac{\mu\theta e^{-\theta^2\rho^2}(\mu\sigma\rho^2 - 6t)}{2\sqrt[3]{\pi}t^3} \tag{A.7}$$

Equation A.7 goes to zero when $\mu\sigma\rho^2 - 6\tau = 0$ or when $\tau = \frac{\mu\sigma\rho^2}{6}$.